Chapter 14

Ion Bombardment-Induced Surface Effects in Materials

Farid F. Umarov and Abdiravuf A. Dzhurakhalov

Additional information is available at the end of the chapter

http://dx.doi.org/10.5772/62731

Abstract

This chapter deals with the experimental research and computer simulation of low- and medium-energy (E_0 = 1-30 keV) ion collisions on the surface of a solid and of the accompanying effects, namely scattering, sputtering, and surface implantation. Experimental and computer simulation studies of low-energy (E_0 = 80–500 eV) Cs^+ ions scattering on Ta, W, Re target surfaces and K^+ ions scattering on Ti, V, Cr target surfaces have been performed for more accurate definition of mechanism of scattering, with a purpose of evaluation of use of slow ions scattering as a tool for surface layer analysis. The peculiarities of the process of correlated small angle scattering of 5–15 keV He, Ne, Ar, Kr, Xe, and Rn ions by the Cu(100), Ni(100), and V(100) single-crystal surfaces have been investigated by computer simulation. It has been shown that under these conditions the inelastic energy losses become predominant over the elastic ones. The anomalous energy losses observed experimentally at the grazing ion scattering by the single-crystal surface were explained. It has been shown by computer simulation that the peculiarities of the chain effect at direct and reverse relation of masses of colliding particles and rainbow effect at quasi-single and quasi-double scattering of ions, heavier than adatoms, lead to the appearance of characteristic peaks in the energy and angular distributions of scattered ions. Analysis of these peaks and comparison with experiment give an opportunity to control the initial stages of adsorption and identification of adsorption structures with the help of low-energy ion scattering. It has been shown that from the correlation of the experimental and calculated energy distributions of the scattered particles, one may determine a spatial extension of the isolated atomic steps on the single-crystal surface damaged by the ion bombardment. Results obtained can be also used to study short-range order in alloys undergoing ordering. Grazing ion-sputtering processes of Si(001), SiC(001), and Cu_3Au(001) surfaces at 0.5–5 keV Ne^+ bombardment have been studied by computer simulations. A preferential emission of Cu atoms in the case of Cu_3Au (001) surface sputtering is observed. It was shown that in the case of grazing ion bombardment, the layer-by-layer sputtering is possible, and its optimum is observed within the small angle range of the glancing angles near the threshold sputtering angle. The peculiarities of trajectories, ranges, and energy losses of low-energy different-mass ions channeling in thin single crystals of metals and semiconductors have been thoroughly studied by computer simulation. It has been

found that in the case of light ions, even at low energy, the main contribution to energy loss is made by inelastic energy losses, whereas for heavy ions, already at $E < 10$ keV, elastic energy losses exceed inelastic ones. Profiles of the distribution of channeled ions have been calculated depending on the crystal lattice type, kind of ions, and their energy. It has been shown that the channeling of low-energy ions through thin single-crystal metal films can be used to determine the sort and adsorption site of light atoms adsorbed on a clean rear surface.

Keywords: ion scattering, sputtering yield, layer-by-layer sputtering, surface implantation, surface channeling, computer simulation, grazing ion bombardment, elastic and inelastic energy losses, vacancy and atomic steps defects on the surface, method of layer-by-layer analysis of single-crystal surface, ***PACS codes:*** 79.20.Rf; 79.20.Ap

1. Introduction

The ion scattering, sputtering, and implantation processes have been the subject of both scientific investigations for a long time and recent rapid developing thin-film technologies and nanotechnologies. These processes underlie such well-known methods of surface science as Ion Scattering Spectroscopy (ISS), Ion Beam Analysis (IBA), Secondary Ion Mass Spectrometry (SIMS), and Ion Beam Modification of Materials (IBMM). Physically, the energy range under consideration is characterized by the dominance of elastic over inelastic energy losses, and by the possibility of considering classical binary collisions using single-center potentials and disregarding the binding energy of the scattering ion in the crystal lattice. The first of these factors determines the upper, and the second, the lower boundary of the energy range. Speaking about the surface, one should bear in mind that the bulk of the solid also participates in the process of ion scattering. The scattering depth is greater, as the ions are lighter and their energy is higher. In this energy range, heavy low-energy ions are scattered practically by one or two atomic layers. This is a great asset since it offers a possibility of using simple models of single and double scattering, and under grazing incidence, of calculating scattering produced only by surface atomic rows and the semichannels, formed by them. The possibility of probing only one surface atomic layer by heavy-ion scattering is also unique and does not have analogs in the other methods of the surface diagnostics of solids. Particle bombardment of a clean and adsorption-covered solid surfaces leads to radiation-induced vacancy defects, atomic steps, and defect clusters, as well as to an atomic scale relief (<100 Å) formation. The concentration and the type of the radiation defects being formed depend upon the experimental conditions and significantly influence the particles' trajectories and their angular and energy distributions, as well as the number of scattered particles. Moreover, there is a correlation between the defect type, the blocking angles of the reflected beam and the energy distributions of the scattered particles, which allows the determination of the defect type and its surface concentration [1–5]. For the analysis of the first one or two atomic top layers of a solid, noble gas ions with primary energies between about 0.5 and 10 keV are very well suited. This is due to their comparatively large scattering cross sections (of the order of 10^{18} cm^2 /sr) and due to the effective neutralization of ions that penetrate into the sample. Thus, the detection of scattered ions provides

a powerful tool for surface analysis that is exclusively sensitive to the outermost atomic layers. The method is known in the literature as "ion scattering spectroscopy" (ISS) [6].

The sputtering process has been the subject of both scientific investigations for a long time and recent rapid developing micro- and nanotechnologies. Processes such as plasma etching and sputter deposition that involve ion bombardment at relatively low (~100 eV) ion energies are widely used in semiconductor processing [7]. Though sputtering and surface modifications of single crystals are widely studied, there are not sufficient data in the case of grazing incidence. However, using glancing-angle ion bombardment for surface modification rather than conventional near-normal incidence ions allows expanding the energy range up to ~10 keV, and has the advantages of reducing damage (such as crater formation) and preferentially removing surface asperities [8] leading to flat surfaces. This is due to the peculiarities of sputtering processes at grazing incidence [9]. Si and SiC crystals have a great importance because of their use in semiconductor technologies. Especially, silicon carbide exhibits a large band gap, a higher breakdown field, a higher thermal conductivity, and a higher saturation velocity, compared to widely used silicon. Besides, SiC is a promising shielding material in nuclear fusion systems such as limiters in Tokamak devices, where the surface erosion is also important [10, 11]. In ref. [12], atomically clean and flat Si(100) surfaces suitable for nanoscale device fabrication were prepared by wet-chemical etching followed by 0.3–1.5 keV Ar ion sputtering. It was found that wet-chemical etching alone cannot produce a clean and flat Si(100) surface which can be achieved by subsequent 300 eV Ar ion sputtering at room temperature followed by a 700°C annealing. Application of grazing angles of incidence of ions on the solid surface opens new perspectives in the investigation of composition, structure, and topography of real surfaces and their modification and polishing by ion beams. Sputtering yields of crystalline silicon carbide and silicon have been experimentally determined, and the results have been compared with Monte Carlo simulations for Ne^+, Ar^+, and Xe^+ ion bombardment in the energy range of 0.5–5 keV under 60° sputtering with respect to the surface normal [13]. The simulation results depend strongly on the input parameters which are not well known, especially for SiC. The TRIM simulation fits the experimental results very well. The evolution of surface morphology during ion beam erosion of Si(111) at 500 eV Ar^+ ion bombardment (60° from normal, 0.75 mA/cm^2 collimated beam current) was studied over a temperature range of 500–730°C [14]. Keeping ion flux, incident angle, and energy fixed, it was found that one-dimensional sputter ripples with wave vector oriented perpendicular to the projected ion beam direction formed during sputtering at the lower end of the temperature range. For temperatures above approximately 690°C, growth modes both parallel and perpendicular to the projected ion beam direction contribute to the surface morphological evolution. Thus, though sputtering and surface modifications of single crystals are widely studied, there are not sufficient data in the case of grazing incidence.

Ion implantation has become a very important technique for modifying surface and impurity doping of semiconductors [15–17]. The ion implantation processes lead to the change of a profile of composition and structure of the subsurface layers. Using glancing-angle ion implantation for surface modification rather than conventional near-normal incidence ions allows expanding the energy range up to ~10 keV and has the advantages of reducing damage

(such as crater formation) and preferentially removing surface asperities leading to flat surfaces. Channeling of low-energy ions in metal and semiconductor single crystals offers the opportunity to create the method of local ion implantation in ultrathin film nanotechnology and surface nano-engineering. Therefore, ranges, energy losses, and profiles of distribution of low-energy ions channeling in crystals have received considerable experimental and theoretical interest [18–20]. For small crystal depths, the approaches which are used in the analytical theory of orientation effects on the large depths become unacceptable, and a computer simulation method for the channeling process modeling appears to be the most preferable [21, 22]. So, the theoretical investigation of atomic collision processes in crystals caused by particle irradiation and deposition is usually done using computer simulation, because real physical conditions (e.g., complicated interatomic interaction potential, surfaces, interfaces, defects, etc.) can be taken into account much easier than it is possible by using analytical methods [17, 21–23].

2. Experimental

The measurements of differential energy spectra and angular distributions of scattered ions were performed in experimental equipment (energy analyzer of the spherical deflector type) with high angular ($\Delta\psi \cong 0.6^{o}$) and energetic ($\Delta E/E \cong 1/125$) resolutions and with the capability to analyze the secondary ion masses by means of time-of-flight technique [24, 25]. The experimental setup includes a UHV scattering chamber with the oil-free pumping system and a base pressure in the 10^{-9} Torr range. During the measurements, the working pressure rises to about 5×10^{-9} Torr. Ions of alkaline metals were obtained in a thermal ion source with a target density of current $J_0 = 5 \cdot 10^{-7}$ A•cm^{-2} under operating conditions. The repeated cycles of an electron bombardment was used for cleaning the target surface. Beams of E_0 = 50–500 eV of Cs^+ and K^+ ions, with a current density $J_0 = 5 \cdot 10^{-7}$ A•cm^{-2}, scattered from clean Ta, W, Re and Ti, V, Cr polycrystal surfaces under an incidence angle of $\psi = 55°$. At the registration of spectra from contaminated targets, the peak of the straight flight was constantly observed. This peak corresponded to the energy of primary ions E_o, that is, the reflection from oxide film which behaved as a screen. After cleaning by electron bombardment, this peak disappeared and bell-shaped spectra were observed. The incident and scattering beams were laid in the same plane, perpendicular to the surface of the target in the point of incidence of ions. The size of ion spot on the sample at normal incidence of ions on the surface was 2 mm, and the scatter of angles of incidence of the ion beam did not exceed $\Delta\psi = \pm 2°$. The backscattered ions are collected at a scattering angle $\theta = 70°$. The angular resolution of the device is $\Delta\theta = \pm 2°$. Usually, within the method of ion-scattering spectroscopy, the interpretation of both angular and energy distribution of the scattered heavy alkali ions (K, Cs) is based on the differential cross section of scattering only, the ionization degree η^+ being 100% [26]. The measured energy spectra were processed by computers for averaging of statistical fluctuations of impulse registration with the use of low-frequency digital filter of Spencer. Repeating the deflection of the voltage on the plate of energy analyzer with alteration of cleaning of the target, the impulse

http://dx.doi.org/10.5772/62731

analyzer was functioning in the mode of accumulation, and summed spectra were registered on the display and digitally printed [24, 25].

3. Computer simulation method

The theoretical investigation of atomic collision processes in crystals caused by ion irradiation is usually done using computer simulation, because real physical conditions (e.g., complicated interatomic interaction potential, surfaces, interfaces, and defects) can be taken into account much easier than it is possible by using analytical methods [4, 5]. The simulation used in our calculations to construct the trajectories of the ions or projectile scattered by target atoms is based on the binary collision approximation [5] with two main assumptions: (1) only binary collisions of ions within target atoms or between two target atoms are considered, and (2) the path in which a projectile goes between collisions is represented by straight-line segments (**Figure 1**). In the binary collision model, particles move along straight-line segments, representing asymptotes to their trajectories in laboratory system, and one determines not a particle trajectory but rather the difference between the angles characterizing the initial and final directions of motion. While this approach permits one to cut the required computer time (compared with direct integration of the equations of motion), it also entails a systematic error due to the fact that over short segments of path, the real ion trajectory differs from the asymptotes used to replace the former. This error was estimated in ref. [27] for the Cu–Cu pair, for a number of potentials and three values of energy. It was established that the deviation of an asymptote from the real trajectory is essential only for head-on collisions and high energies.

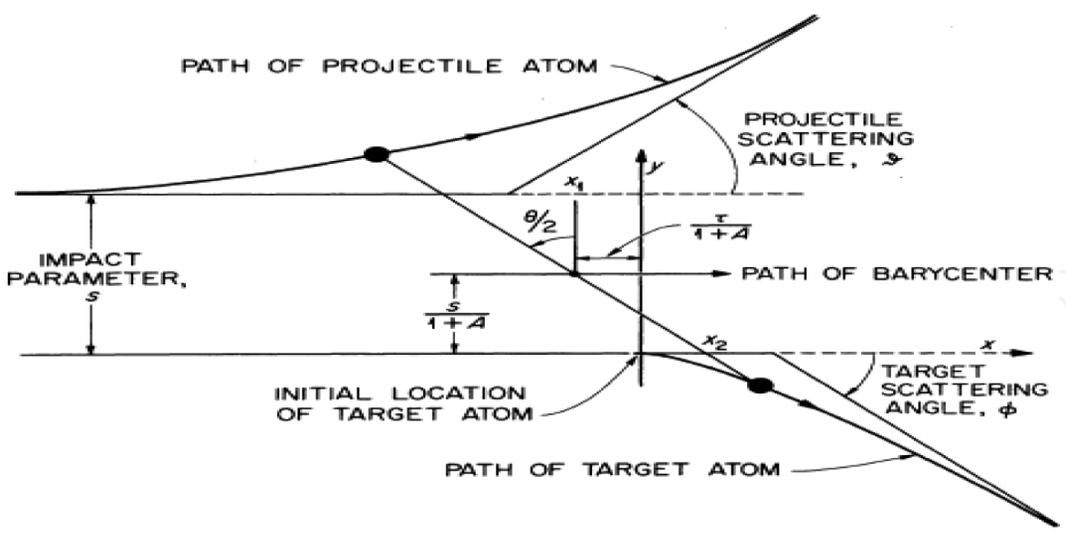

Figure 1. Scheme of the binary collision approximation [27].

For the description of the particle interactions, the repulsive Biersack–Ziegler–Littmark (BZL) potential [28] with regard to the time integral was used. The BZL approximation for the screening function in the Thomas–Fermi potential takes into account the exchange and

correlation energies, and the so-called "universal" potential obtained in this way shows good agreement with experiment over a wide range of interatomic separations. Elastic and inelastic energy losses have been summed along trajectories of scattered ions. The inelastic energy losses ε (E_0, p) were regarded as local depending on the impact parameter p and included into the scattering kinematics. These losses have been calculated on the basis of Firsov model modified by Kishinevsky [5] and contain direct dependence on the impact parameter:

$$\varepsilon\left(E_0, p\right) = 0.3 \times 10^{-7} v Z_1 \left(Z_1^{1/2} + Z_2^{1/2}\right)\left(Z_1^{1/6} + Z_2^{1/6}\right) \left[1 - 0.68 V\left(r_0\right)/E_r\right] / \left[1 + 0.67 \sqrt{Z_1} r_0 / a_{TF}\left(Z_1^{1/6} + Z_2^{1/6}\right)\right] \tag{1}$$

where v and E_r are the velocity and energy of relative atomic motion, Z_1 is a greater, and Z_2 the smaller of the atomic numbers, and r_0 is in units of Å.

The expressions for the ion E_i and recoil E_r energies after binary collision, taking into account inelastic losses, can be written as follows [29]:

$$E_i = \left(1+\mu\right)^{-2} E_0 \left(\cos\theta_i \pm \sqrt{\left(f\mu\right)^2 - \sin^2\theta_i}\right)^2,$$

$$E_r = \mu\left(1+\mu\right)^{-2} E_0 \left(\cos\theta_r \pm \sqrt{\left(f\right)^2 - \sin^2\theta_r}\right)^2 \tag{2}$$

where $f = [1 - (1 + \mu)/\mu\varepsilon(E_0, p)/E_0]$; θ_i and θ_r are the angles of ion and recoil scattering in the laboratory system of coordinate; E_0 is initial energy of impinging ion; p is impact parameter, and $\mu = m_2/m_1$. In ref. [29] the dependencies of $\varepsilon(E_0, p)$ on the basis of the Firsov, Kishinevsky [5], and Oen-Robinson [21] models for $Ne^+ \rightarrow$ Ni pair and low-energy E_0 = 1–10 keV have been calculated. Estimating the accuracy of models for various values of the impact parameter in the low-energy range, it is necessary to notice that in a small impact parameter region ($p < 0.5$ Å), it is more preferable to use the Kishinevsky model; however, in the region of large impact parameters, all three models give approximately the same results, and they are useful even when the energy $E_0 \sim 100$ eV. The above-mentioned models were checked experimentally more than once. On the whole, experimental data agree well with these theories; however, in some cases, the calculated values exhibit discrepancies from the measurement which reach 30–40% [21, 27]. In order to consider simultaneous collisions of a particle with the atoms of the adjacent chains, the procedure proposed in ref. [27] was used. The inclusion of the thermal vibrations assumed that the target atoms oscillated independently of one another, and their deflections from the equilibrium position are subject to the normal Gaussian distribution.

Sputtering has been simulated in the primary knock-on regime. Only the primary knock-on recoil (PKR) atoms ejected from first, second, and third layers have been considered. The presence of planar potential energy barrier on the surface was taken into account. The number of incident ions is 4×10^4. Each new particle is incident on a reset, pure surface. The incident

ions and the recoil atoms were followed throughout their slowing down process until their energy falls below a predetermined energy: 25 eV was used for the incident ions, and the surface binding energy was used for the knock-on atoms. The calculations were performed on the crystals comprising up to 120 atomic layers. The simulations were run with the crystal atoms placed stationary at equilibrium lattice sites.

The channeling simulation program used in the present work is similar by structure to the well-known MARLOWE program and based on the binary collision approximation. But in the case of the solid phase, the binary interaction gets distorted by the influence of neighboring atoms and multiple collisions. It is impossible to calculate inelastic energy losses in this case without exact knowledge of the trajectory of scattering ions. For their calculation, it is necessary to perform computer simulation of ion scattering and channeling in a single crystal. A parallel, uniform, mono-energetic ion beam impinges on an impact area on the surface of a crystal. The angle of incidence of primary ions ψ was counted from a target surface. It is assumed that the incident beam is of small density; so, the ions of the beam do not hit twice at the same place. The impact area covers an elementary cell in the transverse plane of channel axis. The number of incident particles is 4×10^4. The shape of the target area is chosen such that by translating it, one could cover the entire surface of the crystal. Successive multiple scattering of ions from atoms in the rows lying along the principal crystallographic axes is followed in a special search procedure to find the next lattice atom or atoms with which the projectile will interact, with impact parameters for all target atoms forming the walls of a channel calculated for each layer in the crystallite. Around the colliding target atom, the coordinates of the nearest neighbor atoms are consistently set according to the crystal structure of the target. For each set of atoms, the following conditions are checked: (i) it should be at the front part of the ion movement, relatively to a crossing point of asymptotes of the projectile movement directions before and after collision; (ii) the ion impact parameter should be less than p_{lim} (p_{lim} is the impact parameter corresponding to the scattering angle of 0.05°); (iii) among colliding atoms, it should be the first in turn $p_1, p_2, p_3 \ldots$ on the consecutive collisions. After each collision, the scattering angle, energy, and the new movement direction of the channeled ion are determined. It is checked if the projectile is still moving in the given channel. The coordinates of dechanneling are used to obtain the dechanneled and channeled fractions as functions of the depth. The incident ions were followed throughout their slowing-down process, until their energy falls below 25 eV.

In order to consider simultaneous and nearly simultaneous collisions of a particle with the atoms of the adjacent chains, the special procedure proposed in ref. [27] was used. So-called simultaneous collisions which occur if a projectile has a symmetrical position, and which can collide with more than one target atom at the same time, are approximated by successive binary collisions. The inclusion of the thermal vibrations assumed that the target atoms oscillated independently of one another, and their deflections from the equilibrium position are subject to the normal Gaussian distribution. The effect of correlation is equivalent to a reduction of the vibration amplitude of about 5–10%, depending on the effect being looked at [5]. The program allowed the consideration of main peculiarities in channeled particle distribution with depth, such as collision-by-collision details of trajectories, flux-peaking, and difference in specific energy losses for random and channeled trajectories. The number of incident ions

is 4×10^4. Each new particle is incident on a reset, pure surface. The incident ions and the recoil atoms were followed throughout their slowing-down process until their energy fell below a predetermined energy: 25 eV was used for the incident ions, and the surface-binding energy was used for the knock-on atoms. The calculations were performed on the crystals comprising up to 120 atomic layers. The simulations were run with the crystal atoms placed stationary at the equilibrium lattice sites.

The initial energy of incident ions was varied from 0.5 to 10 keV, a grazing angle of incidence ψ counted from the target surface was 3–30°, and an azimuth angle of incidence ξ realized by rotating the target around its normal and counted from the <100> direction was 0–180°. The polar scattering angle θ was counted from the primary beam direction, the polar escape angle δ—from the target surface, and the azimuthal scattering angle φ—from the incidence plane.

In **Figure 2**, the scattering geometry and scheme of a semichannel on the Cu(100) face along the direction <110> and the target area on it are shown. The impact points on the crystal surface filled a rectangle, whose sides were divided into 100 segments in the beam incidence plane (*I*-coordinate) and 1000 segments in the perpendicular direction (*J*-coordinate). The sizes of the target area were 1.28 Å (half-width of the semichannel) on the *J*-coordinate and 2.56 Å (the interatomic distance along the <110> row) on the *I*-coordinate. A substantial part of the calculations presented in this chapter was made by the computer simulation technique. This was required by the complexity of the scattering, sputtering, and channeling trajectories and by a large number of correlated collision events which prohibit the use of statistical stochastic methods of calculation. Mathematical experiment is similar in some extent to the physical one, while permitting us to extract more information from the latter.

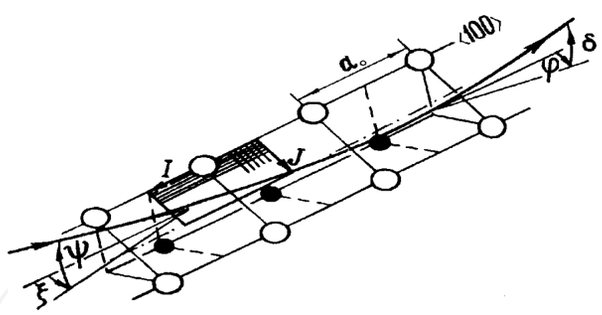

Figure 2. Scheme of ion scattering by a surface semichannel on the Cu(100) face and target area located on it. *I* and *J* are the coordinates of the impact points along and transverse to the semichannel axis, respectively, determining the number of incidence ions [5].

4. Results and discussion

4.1. The low-energy ion scattering by a single and polycrystal surfaces

The peculiarities and mechanism of the low-energy ion scattering by polycrystal targets were experimentally investigated. In refs. [30, 31], the study of low-energy (E_0 = 80–500 eV) Cs^+

and K^+ ions scattering on the surfaces of Ta, W, Re and Ti, V, Cr polycrystal surfaces has been performed experimentally and by means of computer simulation method for more accurate definition of the mechanism of scattering and the evaluation of an opportunity to use heavy ions scattering as a tool for surface layers analysis. The angles of incidence $\psi = 55^0$ and scattering $\theta = 70^0$ correspond to the specular reflection case. In **Figure 3**, the measured differential energy spectra of scattering ions for pairs $Cs^+ \rightarrow Ta$, $Cs^+ \rightarrow W$, $Cs^+ \rightarrow Re$, as well as $K^+ \rightarrow Ti$, $K^+ \rightarrow V$, $K^+ \rightarrow Cr$, in the initial energy range from $E_0 = 80$ to 500 eV, and the target temperature $T = 1250$ K are shown. Some physical parameters of investigated samples at $\mu > 1$ are given in **Table 1**. The same picture can be seen for the case of V, where $E_b^{V} = 5.3$ eV/atom, but E_b^{Ti} and E_b^{Cr} are 4.86 and 4.10 eV/atom, respectively.

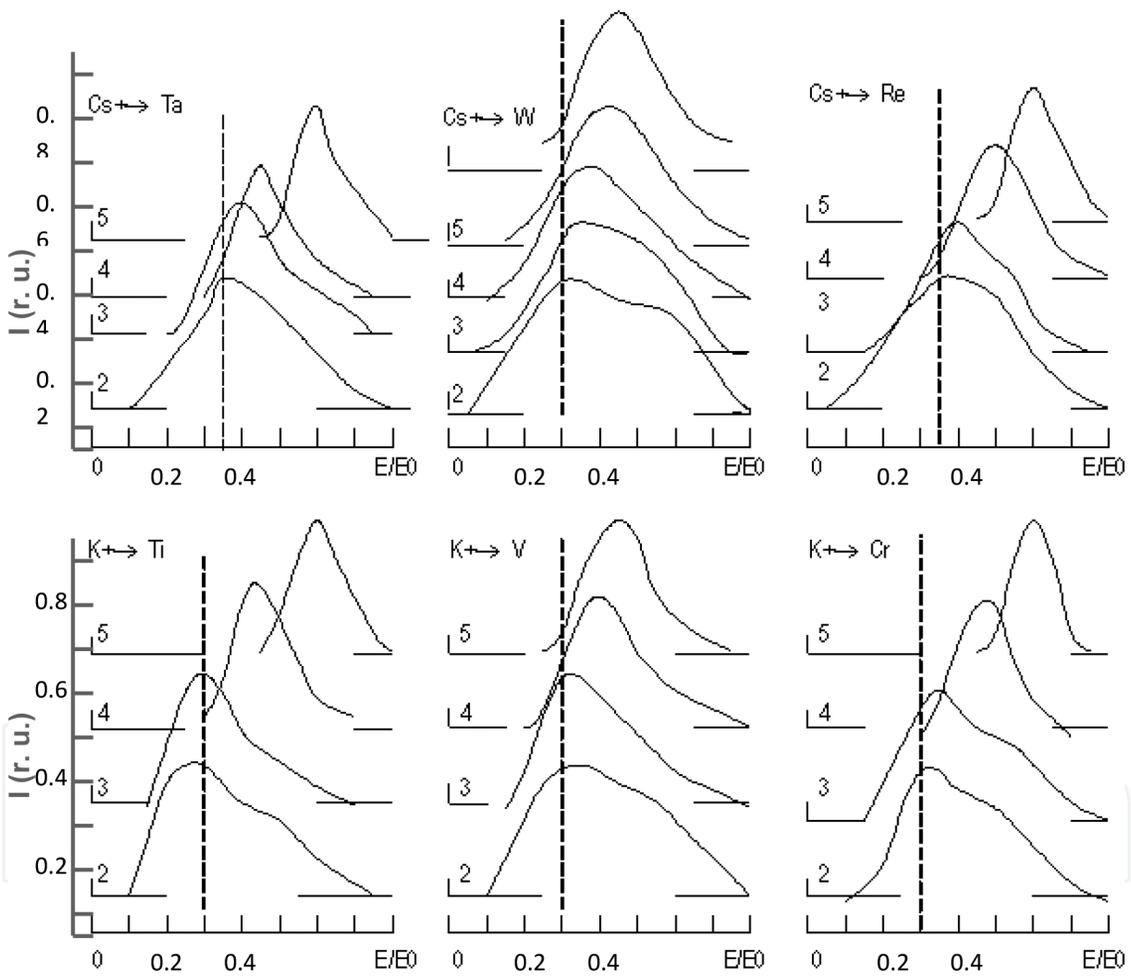

Figure 3. Differential energy spectra of Cs^+ and K^+ ions scattering on corresponding polycrystalline targets at E_0 (eV) = 500 (1); 400 (2); 200 (3); 100 (4); 80 (5). Dashed line shows the calculated results under the formula (3).

Here $\mu = m_2/m_1$ is the mass ratio of target atom and ion, respectively. It is seen that the form of spectra in all the cases is similar. It is characterized by a peak in the low-energy range. When E_0 decreases, the position of the maxima of energy spectra shifts toward greater relative energy retained by ions. This shift is the smallest in the case of W when the binding energy of target

atoms is E_b^{W} = 8.66 eV/atom, and we shall note that for Ta the binding energy is E_b^{Ta} = 8.089 eV/atom and for Re, E_b^{Re} = 8.10 eV/atom.

The position of the maxima in the binary collision approximation (energy of scattered ion retained at single collision with target atom) can be defined approximately as follows [32]:

$$E / E_0 = \{\left[\cos\theta \pm \sqrt{(m_2 / m_1)^2 - \sin^2\theta}\right] / [1 + m_2 / m_1\}^2 \quad (3)$$

where E is the relative energy of the scattering ions which suffered a single binary collision with a target atom (dashed lines in Figure 3), E_0 is the energy of primary ions, and θ is the angle of scattering. In Figure 3, one can notice the shift of the maxima from the calculated position. As we can see, this shift depends on the binding energy of target atoms and initial energy of scattered ions. Let us note that in case of binary elastic collisions, the energy retained by the scattering ion, at the given angle of scattering, depends on the mass ratio of colliding particles, and the position of the maxima of the energy spectra should be kept constant.

Ions	**Cs^+ (m_1 = 132.90 a.u.)**			**K^+ (m_1 = 39.10 a.u.)**		
Targets	Ta	W	Re	Ti	V	Cr
Mass m_2 (a.u.)	180.95	183.85	186.20	47.90	50.94	51.99
Mass ratio ($\mu = m_2/m_1$)	1.36	1.38	1.40	1.23	1.30	1.33
Binding energy (eV/atom)	8.09	8.66	8.10	4.86	5.3	4.10
Melting temperature (°C)	2996	3387	3180	1660	1900	1857

Table 1. Some physical parameters of investigated samples at direct mass ratio of colliding particles $\mu > 1$.

In **Figure 4a and b**, the dependencies of relative energy retained by scattering ions E_m/E_0 in the maximum energy distributions of Cs^+ and K^+ ions scattered by Ta, W, Re and by Ti, V, Cr polycrystals, respectively, versus the initial energy of impinging ions are presented. It is seen in the whole investigated range of primary energies E_0 that the significant growth of relative energy E_m/E_0 (where E_m is the energy of scattering ions in a maximum energy distribution) with E_0 decrease is observed. The curves for targets with close values of binding energy E_b practically coincide, and it may be observed that this growth of relative energy for vanadium and tungsten is flatter. Thus, the least increase in the relative energy of scattered ions E_m/E_0 with decrease of initial energy E_0 occurs for targets with the largest binding energy E_b (8.66 eV/atom for W and 5.3 eV/atom for V), correspondingly. Violation of the binary character of interaction at initial energy decrease began for these pairs at $E_0 \approx 200$ eV. For other pairs with smaller binding energy of target atoms, this breach began at $E_0 \approx 400$eV.

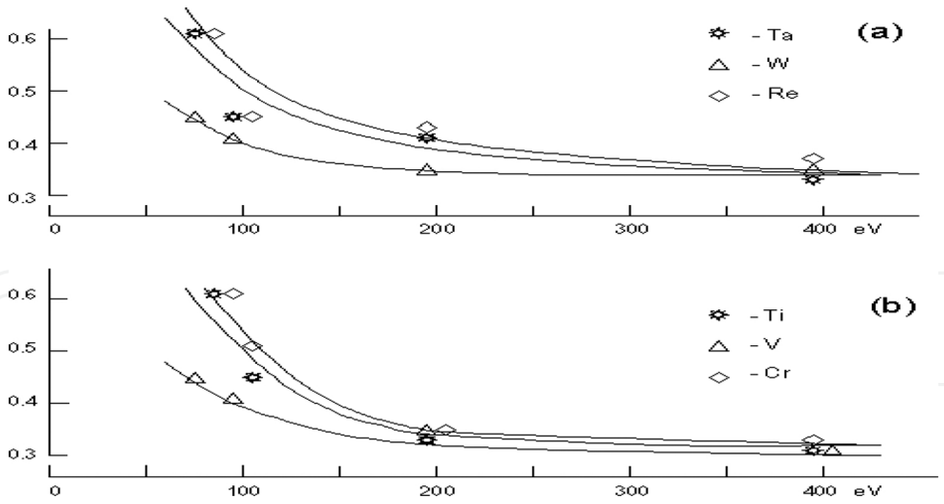

Figure 4. Dependencies of relative energy E_m/E_0 retained by scattering Cs^+ (a) and K^+ (b) ions in a maximum of energy distribution versus the initial energy of impinging ions E_0.

Formerly, it was shown that the picture represented on Figure 4 occurs also for the cases of heavy Cs^+ scattering on the polycrystal surfaces with small atomic masses (Al, Si, Ni) for which the mass ratio of colliding particles is $\mu < 1$ [30]. The angles of incidence $\psi = 45^0$ and scattering $\theta = 90^0$ also correspond to the specular reflection case. In contrast to the results for $\mu > 1$, in cases with $\mu < 1$, the smallest increase of the relative energy of scattered ions E_m/E_0 with decrease of initial energy E_0 occurred for the Al target with the smallest binding energy E_b.

In ref. [30], we showed that at an inverse mass ratio of colliding particles ($\mu < 1$), for example, Cs^+ on Al ($\mu = 0.20$), the possible scattering angles considerably exceed a limiting scattering angle in a single collision ($\theta_{lim} = \arcsin \mu$). For Cs^+ ions scattering on Al target, $\theta_{lim} = 11.7°$. This is possible either in the presence of seven or more successive binary collisions of ion with target atoms. This is not probably at that low energy, or at the interaction of an impinging ion Cs^+ with the several bonded between each other surface Al atoms simultaneously. The determined correlation between relative energy suffered by scattering ions and binding energy of target atoms confirms such many-particle character of interaction. As established in refs. [30, 31], contrary to the scattering results on targets with direct mass ratio $\mu > 1$ (Figure 2), in the cases with inverse mass ratio $\mu < 1$ the smallest increase of the relative energy of Cs^+ scattered ions E_m/E_0 with decrease of initial energy E_0 occurs for the Al target with the smallest binding energy ($E_b = 3.34$ eV/atom; $\mu = 0.20$). For Co, Si и Ni targets, binding energies are 4.387, 4.64, and 4.435 eV/atom, correspondingly. In both cases, the curves E_m/E_0 (E_0) are placed above each other relative to the binding energies of target atoms to show the influence of binding energy on a process of low-energy ions scattering. There is a correlation between the value of energy change maintained by ions for different values of E_0 in the case of scattering by targets with different masses of atoms (for $\mu > 1$ and $\mu < 1$) and its binding energies. From this contrary behavior between the E_m/E_0 (E_0) dependencies and the target atom binding energy value E_b for cases with direct ($\mu > 1$) and inverse ($\mu < 1$) mass ratio of colliding particles, one can explain the different character of many-particle interaction in these cases [30, 31].

Some physical parameters of the investigated samples at direct ($\mu > 1$) and inverse ($\mu < 1$) mass ratio of colliding particles are presented in **Table 2**. The growth of E_m/E_0 with E_0 decrease, coinciding with the curves for Ta and Re cases in contrast to the scattering by W, as well as the similarity of curves for Ti and Cr cases in contrast to the V case can apparently testify to the nonbinary multiparticle nature of interaction of low-energy Cs^+ and K^+ ions during the scattering by the investigated targets for which $\mu > 1$. The contrary behavior of the E_m/E_0 (E_0) dependencies concerning the target atom binding energy value E_b for cases with direct ($\mu > 1$) and inverse ($\mu < 1$) mass ratio of colliding particles testifies to the different character of many-particle interaction in these cases.

Ions	**Cs^+ (m_1 = 132.90 a.u.)**					
Targets	Ta	W	Re	Al	Si	Ni
Mass m_2 (a.u.)	180.95	183.85	186.20	26.98	28.09	58.70
Mass ratio ($\mu = m_2/m_1$)	1.36	1.38	1.40	0.20	0.21	0.44
Binding energy (eV/atom)	8.09	8.66	8.10	3.34	4.64	4.435
Melting temperature (°C)	2996	3387	3180	660	1420	1452

Table 2. Some physical parameters of investigated samples at direct ($\mu > 1$) and inverse ($\mu < 1$) mass ratio of colliding particles.

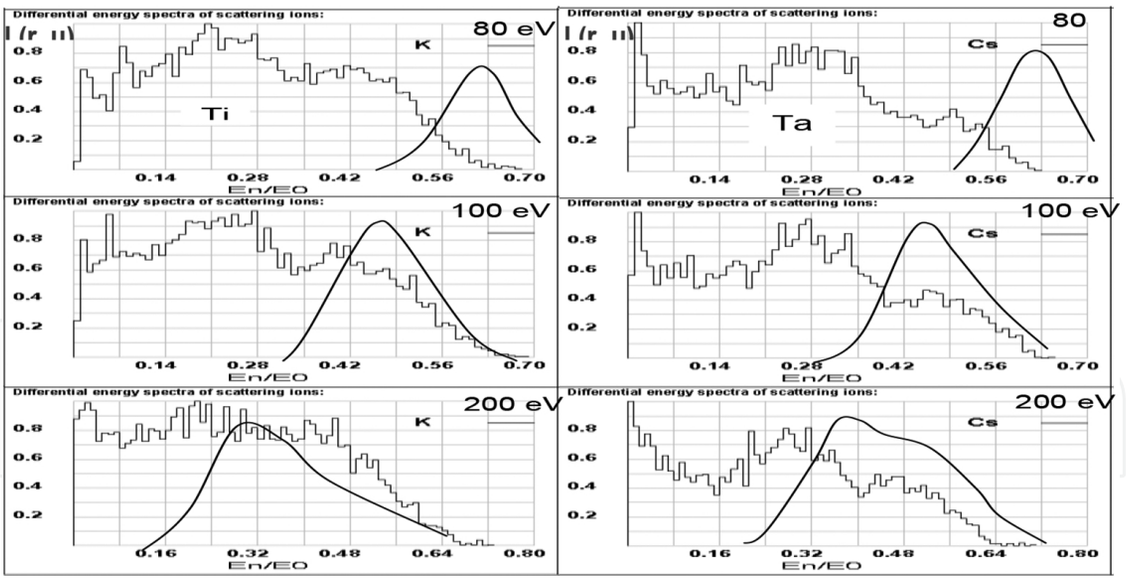

Figure 5. Comparison of experimental energy distribution curves with calculated histograms in the cases of Cs^+ and K^+ ions scattering by Ta and Ti polycrystals, respectively. *I* (r.u)—intensity of the scattered ions in relative units.

The scattering of Cs^+ and K^+ ions on experimentally investigated polycrystals was considered on the basis of binary collision approximation by means of computer simulation to assess the experimentally observed fact of the retaining of abnormally great values of relative energy by scattering ions. The calculations were performed using the visualized CASWIN code [33, 34]

based on the Monte Carlo simulation method and treating the interaction of ions with a solid surface to be within the binary collision approximation. The Ziegler–Biersack–Littmark and "Kr-C" potentials were used. The surface potential barrier for ions was assumed to be null, and the values of binding energies of surface atoms were taken as mentioned above. The comparison of calculated results (histograms) with the experiment for K^+–Ti (left) and Cs^+–Ta (right) is given in **Figure 5**. One can see that the agreement became better when E_0 increased, which confirms that the binary collision approximation is fair at sufficiently high energies.

With E_0 decrease, the maximum of the calculated histogram keeps its position while the experimental curve disposes to the greater relative energy range, significantly at 80 eV. To realize what kind of scattering ions contribute to the peaks observed in the calculated histograms, each case of multiple scattering was separated.

On the basis of the conducted research, the correlation between the value of energy change maintained by ion for different values of E_0 in the case of scattering by targets with different masses of atoms and its binding energies is experimentally established. This correlation indicates considerable influence by the binding of surface atoms to each other on the process of scattering in the low-energy range by polycrystal targets. It is established that low-energy scattering with direct ($\mu > 1$) and inverse ($\mu < 1$) mass ratios of colliding particles is not described by the mechanism of binary elastic interactions. Summarizing the effects revealed in the present research, such as (i) the disappearing of a structure of energy spectra; (ii) high values of relative energy of scattering ions E_m/E_0 and its dependence on initial energy E_0; (iii) dependence of scattering ions' energy on binding energy, mass ratio, melting temperature, and packing density of target atoms, one can draw a conclusion about the multiparticle nature of the interaction. The contrary behavior of the E_m/E_0 (E_0) dependencies concerning the target atom binding energy value E_b for cases with direct ($\mu > 1$) and inverse ($\mu < 1$) mass ratio of colliding particles testifies to the different character of many-particle interaction in these cases. In order to use ion-scattering as a tool for diagnostics of disturbances of elemental composition and structure on atomic scale, it is necessary to use much higher initial energies ($E_0 \geq 1$ keV).

4.2. Anomalous inelastic energy losses and trajectory effects at small-angle ion scattering by single-crystal surface

As is known [35], the elastic mechanism of energy losses is dominant in low- and medium-energy range for ions with atomic numbers $Z \geq 10$. However, under the specific conditions of correlated glancing ion scattering from the single-crystal surface, the reverse pattern becomes possible where the inelastic mechanism will predominate. The reasons for this are the large number of collisions involved and the fact that small impact parameters cannot be reached along the scattered ion trajectory [5]. Inelastic processes of ion interaction with crystal exhibit the so-called trajectory effects. Basically, this means that inelastic processes and the associated inelastic energy losses depend on the actual trajectory of the scattered particle [36]. It turned out that the relative magnitude of the anomalous energy losses depends on crystal orientation and increases with decreasing initial ion energy. In ref. [37], this effect is related to the mechanism of surface hyperchanneling (SHC) which dominates for very small grazing angles.

The present section gives the results of a study of elastic and inelastic energy losses and of the specific features of the ion trajectories appearing in scattering from discrete model potentials on an atomic row, a semi-channel and a channel on the surface of a single crystal at small grazing and scattering angles, as well as of the contribution of the various scattering mechanisms to the experimentally observed anomalous energy losses [5, 38]. Trajectories of 15 keV Ar^+ ions suffering grazing scattering at the atomic chains, semi-channels, and channels on the Cu(100) surface were traced in the uppermost 10 atomic layers by computer simulation. They have been simulated in the binary collision approximation using the Biersack–Ziegler–Littmark interaction potential [35] and with regard to the time integral. In order to consider simultaneous collisions of an ion with several target atoms the procedure proposed in ref. [27] was used. Elastic and inelastic energy losses have been summed along trajectories of scattered ions. The latter one has been calculated on the basis of the Firsov model modified by Kishinevsky [5] and included into the scattering kinematics. Figure 2 shows schematically a semi-channel on a Cu(100) face in the <110> direction and the target area on it. It also identifies the angles used in the computation. The calculations have been performed for target points, covering uniformly (on the I and J coordinates) all surfaces of target area, where the total number of filling ions is equal to 5×10^4.

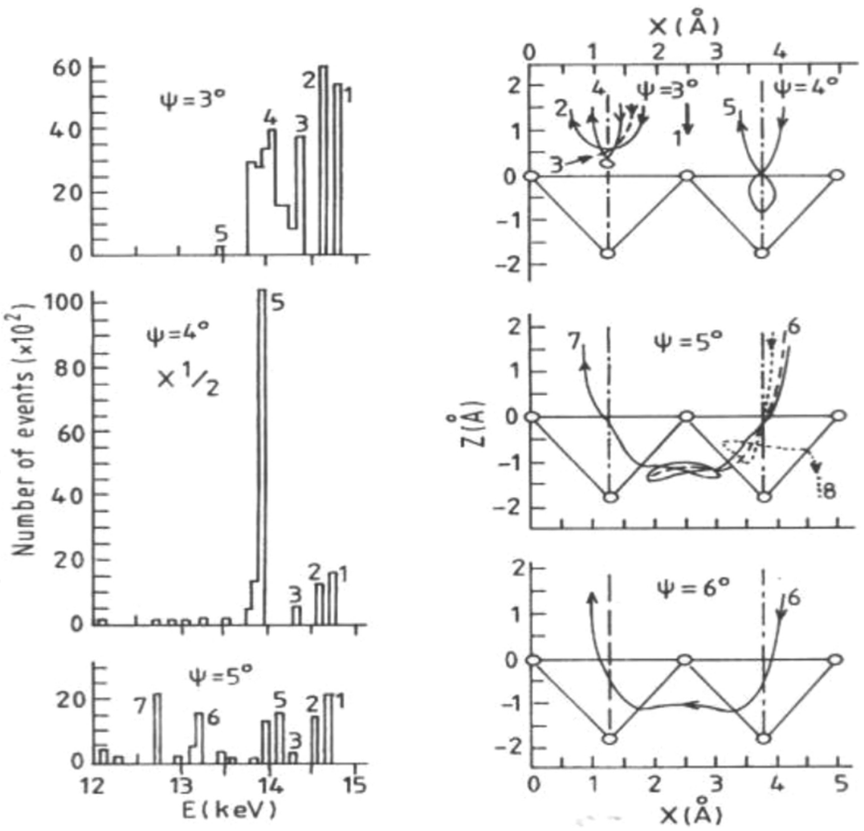

Figure 6. Energy distribution histograms of 15 keV Ar^+ ions scattered specularly ($\theta = 2\psi$) from Cu(100) <110> . On the right-hand side, the most characteristic ion trajectories projected in the transverse plane of the <110> semichannel are depicted.

Figure 6 shows energy distribution histograms for 15 keV Ar^+ ions scattered specularly from Cu(100) <110> into a detector with an angular aperture of ±0.5°. The ions scattered along atomic row ridges contribute to the peaks labeled 1. The peaks located to the left and labeled 2–4 correspond to the ions undergoing surface hyperchanneling (SHC) [37]. In the case of trajectories of type 4, the ions are seen to be focused in the <110> direction, the focus point lying about 0.5 Å above the surface plane. At $\psi = 4°$, the shape of the spectrum undergoes a substantial change because of a sharp increase in the number of trajectories of the new type 5, and a decrease of the contribution from type 1–4 trajectories. The figure shows that the ions with type 5 trajectories are focused by surface rows with the focus point lying slightly above the surface, and propagate afterwards in a diverging flux toward the walls of the semi-channel.

Trajectories of type 5 differ in shape and character from SHC trajectories. The sharp increase in their number suggests the existence of a peculiar refocusing effect which results in a pronounced narrowing of the spatial distribution of scattered particles. The angular range where this refocusing effect is observed is small ($3.5° \leq \psi < 5°$), so that at $\psi = 5°$ it is no more. At $\psi = 5°$, in addition to peaks 1–5, new, lower energy peaks 6 and 7 appear in the spectrum. The pattern of particle motion along type 7 trajectories is more complex than that along trajectories of type 6. In the latter case, the part of the trajectory within the channel is shorter, the particle actually crossing it. In their shapes and general patterns, these trajectories do not belong to those typical for subsurface hyperchanneling [37], which were also observed in our calculations. There also exist trajectories of type 8 corresponding to ions which, on overcoming the potential barrier of the semi-channel walls, penetrate into deeper lying layers and thus are not backscattered.

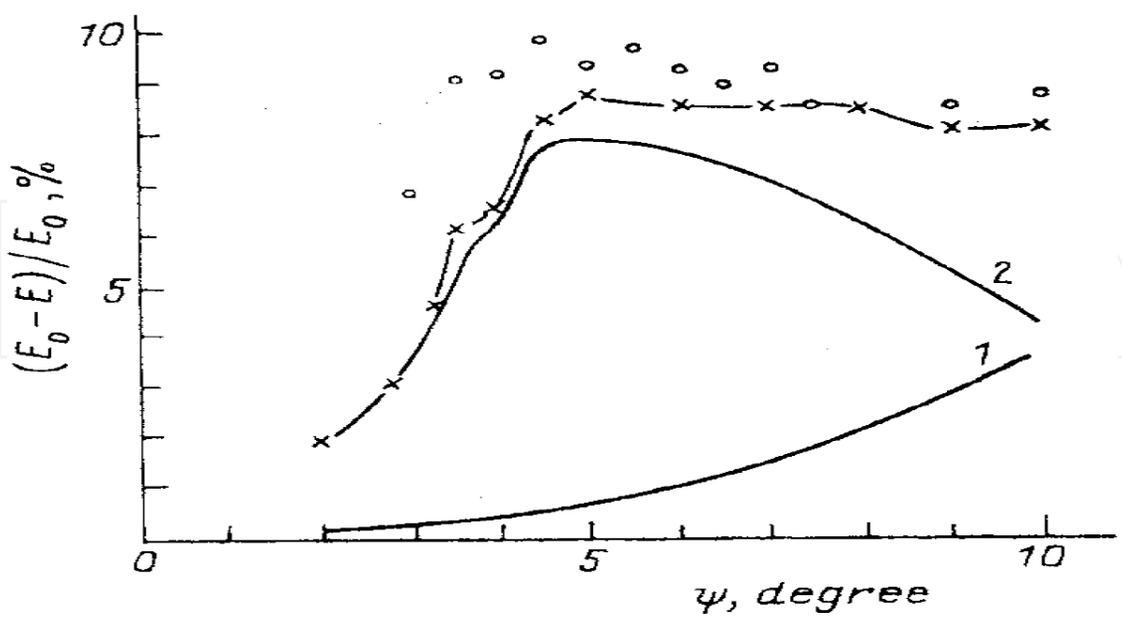

Figure 7. Experimental [39] (circles) and calculated [5, 38] (crosses) dependencies of the relative energy losses versus the grazing angle for the case $\theta = 2\psi$ for 15 keV Ar^+ ions scattered from Cu(100)<110>; elastic (1) and inelastic (2) contributions to the total relative energy losses.

Figure 7 displays experimental [39] and calculated [38] dependencies of the relative energy losses $(E_0 - E)/E_0$ on the grazing angle for 15 keV Ar^+ ions scattered from Cu(100) <110>. Here the circles are the experimental data [39], crosses - calculation [5, 38], 1 - elastic and 2 - inelastic energy losses contributions to the total relative energy losses. The calculated curve was constructed by averaging the losses over the various scattering mechanisms in accordance with their relative contributions to the spectra. As seen from **Figure 7**, the main contribution to the anomalous energy losses comes from inelastic losses. The maximum inelastic energy losses are due to particles with trajectories 5–7, as well as due to those undergoing subsurface hyperchanneling. Thus, the elastic energy losses are considerably smaller than the inelastic ones in a region of glancing scattering. The fact that the inelastic losses exceed the elastic ones for small ψ in the medium energy range is due to an increase in the number of collisions and the particle trajectory length in the surface region, as well as to the absence of small impact parameters in the course of scattering. The predominance of the inelastic energy losses should reveal itself in the efficiency of the various inelastic processes accompanying the glancing ion scattering from a single-crystal surface.

4.3. Low-energy ion scattering by atomic steps on the single-crystal surface

Ion bombardment of a solid surface leads to radiation-induced vacancy defects, atomic steps, and defect clusters, as well as to an atomic scale relief (<100 Å) formation. The concentration and the type of the radiation defects being formed depends upon the experimental conditions

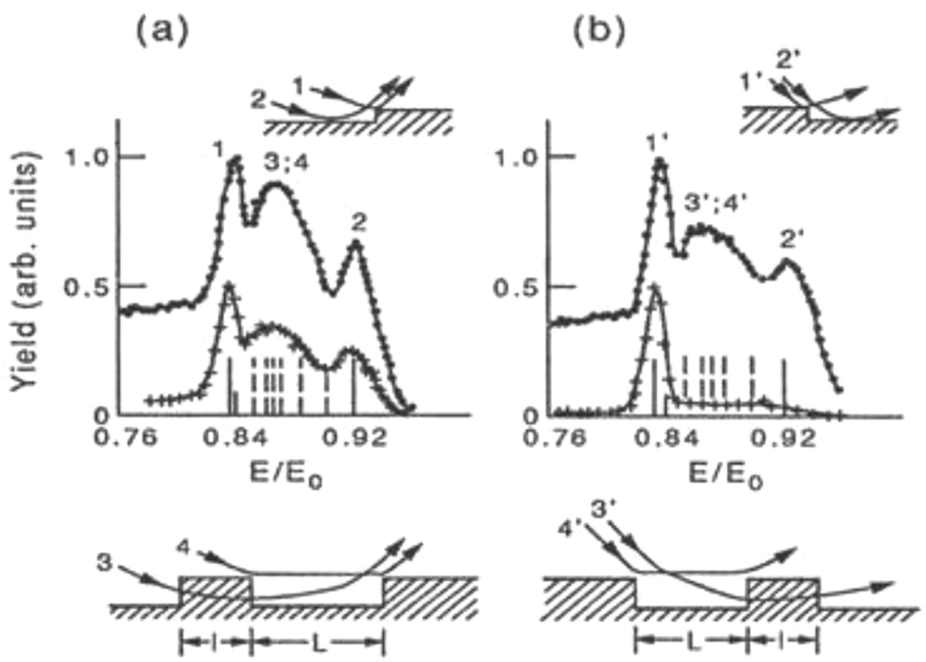

Figure 8. Energy distributions of the total number (.....) and ion component (+++++) of the argon particles scattered at the angle θ = 30° by the surface of Cu(100)<100> at ψ = 7° (a) and 23° (b). The calculated energy positions corresponding to the scattered ions in the spectra are designated by the solid and dotted vertical lines.

and significantly influences the trajectories, angular and energy distributions, as well as the number of the scattered particles. Moreover, there is a correlation between the defect type, the blocking angles of the reflected beam, and the energy distributions of the scattered particles that allows a determination of the defect type and its surface concentration [2–5]. In ref. [40] the number of step atoms formed on the surface of a single crystal Cu(100) at T = 300 K, predamaged by the bombardment with Ar^+ ions, with an initial energy of E_0 = 10 keV and the current density on the target within the range of 10^{-6}–10^{-8} A◎cm^{-2} has been estimated. Figure 1 shows both the energy distributions of the total number (ions plus neutrals) and the ion component of the argon particles scattered by the Cu(100) surface in the <100> direction for two incidence angles of ψ = 7° (a) and 23° (b), and a constant scattering angle of θ = 30°. The particles having undergone the quasi-single scattering on the step atom of the monoatomic semi-infinite steps contribute to the peaks 1 and 1' of the spectrum, and the particles reflected by the step atom with the previous or subsequent specular scattering on the ordered atomic chain contribute to the peaks 2 and 2' [40]. Schematically, such trajectories are shown in the top of **Figure 8**. The number of step atoms has been estimated according to the intensity of the quasi-single scattering peaks in the energy spectrum of the total number of the scattered particles at ψ = 7° (1) and 23° (1'). In **Figure 9**, these spectra are shown with a solid line.

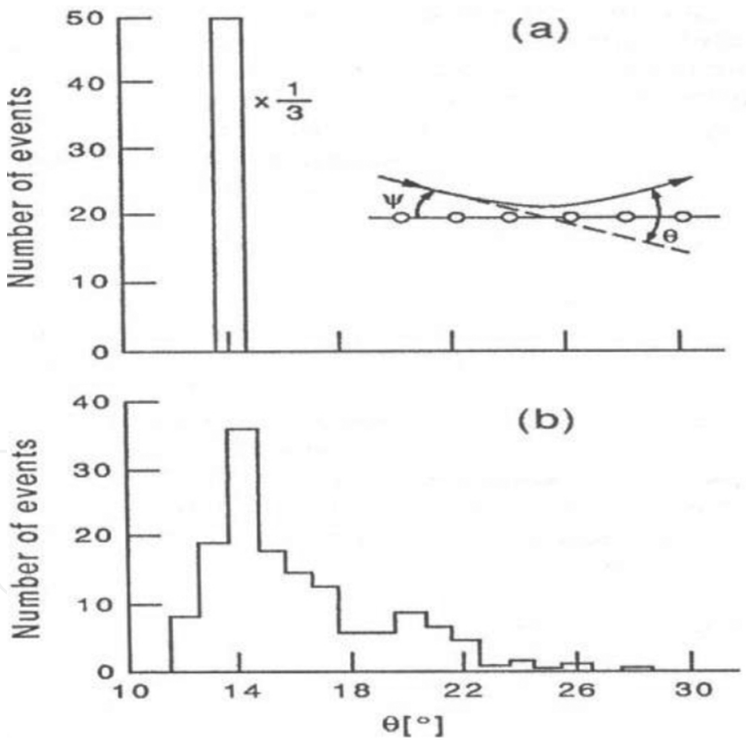

Figure 9. Histograms of the angular distributions of Ar^+ ions with E_0 = 10 keV scattered by the ordered surface of Cu(100)<100> at the incidence angle ψ = 7° for T = 0 (a) and T = 300 K (b).

A possibility of scattering at the angle θ = 30° under small (ψ < 10°) and large (ψ > 20°) incidence angles is conditioned by the fact that the bombardment introduces irregularities into the perfect infinite atomic chain, that is, it becomes finite and is followed with the step-up (a) or down (b).

The number of step atoms formed under ion bombardment , and estimated from the peaks 1 and 1' over the energy spectra, with an accuracy of ~30%, proved to be ~2×10^{14} cm^{-2}.

The aim of the present work is to study the influence of surface atomic steps on the angular and energy distributions of scattered ions, and to determine both the spatial extension of the atomic steps on the damaged surface of a single crystal and the distances between them under experimental conditions [40]. For this purpose, the trajectories of the particles scattered by both the ordered part of the surface and the monoatomic steps of different spatial extensions placed upon it have been studied carefully by means of computer simulation [41, 42]. The computer simulation allowed an investigation of the atomic steps effect on the single-crystal surface upon the trajectory features of the ions being scattered along the ridge of the atomic chains and undergoing the surface hyperchanneling and semichanneling as well.

The calculated energies of the particles scattered along trajectories of the 1, 1', 2, and 2' agreed with the experimentally determined positions of the corresponding peaks in the spectrum, namely: $E/E_0 = 0.84$ and $E/E_0 = 0.92$ (vertical solid lines in Figure1a and b). The ions scattered along the trajectories 2 and 2' before being reflected from the step atom or after it usually underwent 8–10 collisions with the chain atoms. Their range along the surface approximately amounted to 25–30 Å, and the inelastic energy losses were about 20% of the total loss. Broad maxima 3, 4 and 3', 4' between the peaks 1 and 2 as well as 1' and 2' were not explained in ref. [40]. It was suggested in ref. [40] that they could be explained by the particles scattering on the ordered surface, taking into account the thermal vibrations of its atoms. Our calculations have shown, however, that these broad maxima could not be explained in this fashion. In Figure 9, the histograms of the angular distributions of the scattered argon particles at $\psi = 7°$ and the target temperature $T = 0$ (a) and $T = 300$ K (b) are shown. As seen, the scattering at angle $\theta = 30^0$ at $\psi = 7°$ is not observed upon the ordered surface, because of blocking, even taking into account the thermal vibrations of its atoms. Variations in the interaction potential, and in particular the use of the conjugated Firsov and Born–Mayer potential [43] also did not allow an explanation of scattering at $\theta = 30°$ and $\psi = 7°$. In order to explain the maxima 3, 4 and 3', 4' in the spectra, we have calculated the trajectories of the ions scattered on the surface, upon which before or after the semi-infinite monoatomic step and isolated steps (atomic fragments) of different extension l, separated by the parts of the ordered surface of length L, were located. Schematically, such trajectories are shown at the bottom of Figure 8.

The trajectories 3 and 3' contribute to the broad maxima 3, 4 and 3', 4' in the spectra, being formed by two adjacent steps: the particles pass under the first of the steps and then are reflected from the face atom of the second step. The trajectories of quasi-double scattering 4 and 4' on the face atoms of the adjacent steps also contribute to these maxima. In Figure 9, the contributions of the above-mentioned trajectories are designated with vertical dotted lines. It follows from the calculation that the increase of the number of the atoms in the first step (atomic fragment), and consequently, its extension with constant distance between the steps L leads to an energy decrease of the ions being scattered along the trajectories of the 3 and 3' type. A change in the number of atoms in the first step (atomic fragment) from one to four allows 3 and 3' type trajectories of the scattered ions to be obtained with energies covering the whole interval for the relative energies of the broad maxima from $E/E_0 = 0.85$ to $E/E_0 = 0.90$. The steps

(atomic fragments) consisting of two and three atoms separated by the parts of the ordered surface of the length L = 15–45 Å turned out to be the most likely ones. The scattering on such steps contributes to the area of the broad peaks 3, 4 and 3', 4' maximum (E/E_0 = 0.86–0.88). The distances between the atomic steps (fragments) vary from a minimum equal to two lattice constants of Cu(100), to ~45 Å. The presence and value of the peaks 2 and 2' in the spectra confirm the existence of the distance between the steps to be within ~25–45Å. The trajectories of the 4 and 4' type have turned out to be weakly sensitive (by energy value) to the distance between the steps, but their probability sharply decreases with the increase of L. It is of interest to note that the disappearance of the 2', 3', and 4' peaks in the ion component of the scattered flux at ψ = 23° agrees well with the character of the corresponding trajectories. The conclusions concerning the spatial extension of the atomic steps and the distances between them obtained by the use of the conjugated potential turned out to be in good agreement with the results described earlier, obtained by the Biersack–Littmark–Ziegler potential.

Thus, from the comparison of the results of computer simulation of the scattered particles' trajectories with the experimental energy distributions, one can draw a conclusion that for bombardment of a Cu(100) surface with 15 keV Ar^+ ions under the experimental conditions [40], isolated monoatomic steps (fragments) consisting of several atoms (from one to four) are formed upon it. The distances between the steps vary from two lattice constants of Cu(100) to ~45 Å. The most likely ones turned out to be the steps (fragments) consisting of two and three atoms separated by the parts of the ordered surface of the length L = 15–45 Å. The estimated value for the number of the atomic steps calculated by us on the basis of the proposed model of the damaged surface agrees with the value ~2×10^{14} cm^{-2} obtained in ref. [40].

4.4. Small angle ion scattering by structures on the single-crystal surface corresponding to the initial stages of adsorption

Determination of equilibrium position of adatoms, initial stages of adsorption, and the structure of submonolayer adsorption coverages on crystal surfaces are fundamental problems of surface physics. Along with low-energy electron diffraction (LEED), alternative methods are being developed for analysis, in particular ion scattering spectroscopy (ISS) [4, 5, 44]. An attractive peculiarity of the ISS method is its high surface sensitivity, enabling monolayer analysis. The structural analysis of surfaces by this method is based on a comparison of experimentally measured energy and angular distributions of scattered particles with calculations based on a chosen surface model. In this section, small-angle scattering of He^+ and Ne^+ ions with initial energies E_0 = 1–5 keV and grazing angles within the interval ψ = 7.5–15° by Ni(100) <100> single-crystal surface with submonolayer coverages by oxygen or deuterium atoms have been studied. The dynamics of changes of angular and energy distributions from scattering on different adsorption structures, corresponding to the initial stages of adsorption have been studied.

Besides the usual atomic chain effect [5] corresponding to the direct mass ratio of colliding particles, that is, to cases where the mass of projectile m_1 is less than that of an atom in the chain m_2, in our case a situation arises where an adatom is lighter than the projectile ion. The atomic chain effect manifests itself in this case in a number of features associated with the

existence of a limiting scattering angle $\theta_{lim} = \arcsin(m_2/m_1)$ in quasi-single (QS) and quasi-double (QD) collisions, as well as with the fact that scattering at a given angle $\theta < \theta_{lim}$ is possible for two values of the impact parameter p [5, 45]. Oxygen atoms on a metal surface at submonolayer coverages and $T < 300$ K may be adsorbed in two stages—chemisorption and oxide-state. It has been known for many years from LEED [44] that two ordered surface structures can be obtained during the chemisorption of oxygen on Ni(100). A p(2 × 2)–O pattern is obtained at low coverages (one adsorbed oxygen atom for four nickel atoms on the first substrate plane). The saturation of the adsorption corresponds to one adsorbed atom for two nickel atoms and is associated with a c(2 × 2)–O pattern. For our p(2 × 2)–O and c(2 × 2)–O on Ni(100) calculations, we place the O atoms in the fourfold center sites at a distance 0.9 ± 0.1 Å above the Ni surface plane as found in LEED analysis [44] (**Figure 10a–c**).

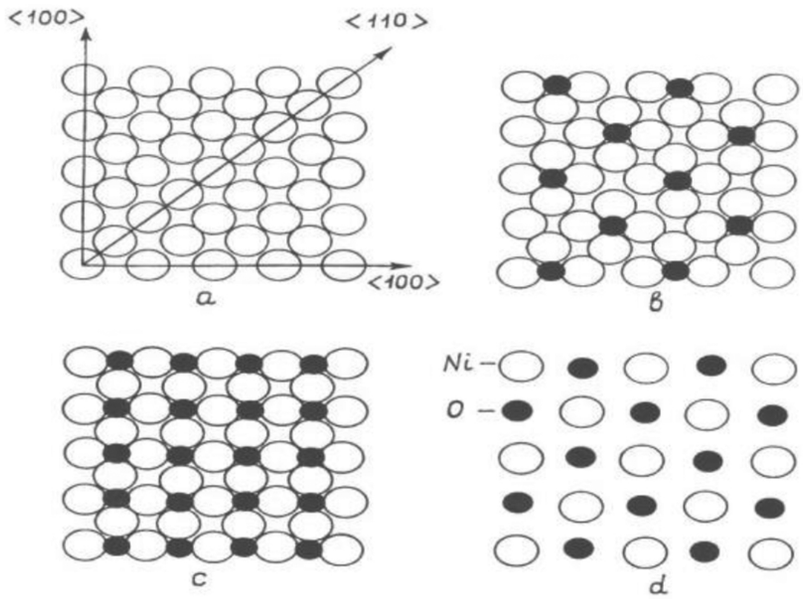

Figure 10. Position of Ni atoms in the first layer of Ni(100) (a) and oxygen atoms in adsorption structures, corresponding to initial stages of adsorption: (b) p(2 × 2); (c) c(2 × 2); (d) NiO(100) (1 × 1).

Adsorption structures p(2 × 2)–O and c(2 × 2)–O on the Ni(100) surface form sequentially and do no lead to substrate reconstruction [44]. At further increase in oxygen exposure and a coverage degree of 0.62, NiO(100)–(1 × 1) oxide islands begin to form with the NaCl type structure (Figure 1(d)). At the initial stages, this process is interpreted as a phase transition of the first order, and unlike chemisorption it is accompanied by a shift of substrate atoms. In Figure 11, histograms of energy distributions of Ne^+ ions, experiencing specular scattering on chains of atoms on a clean Ni(100)<100> surface and on surfaces with different adsorption structures are presented. The acceptance of the analyzer collecting scattered particles, constituted by polar and azimuthal scattering angles is $\Delta\theta = \Delta\varphi = \pm 0.5°$. In a case of a clean surface (**Figure 11a**), the usual peaks of QS- and QD-scattering (1,2) are observed. At specular scattering on the structure p(2 × 2)–O (**Figure 11b**), three peaks, two of which (3 and 4) are of peaks of QS-scattering on oxygen atoms with impact parameters p, smaller and larger p_{lim}

accordingly are present in the spectrum. Here $p_{\lim}(E_0)$ is the impact parameter corresponding to scattering at a limiting angle.

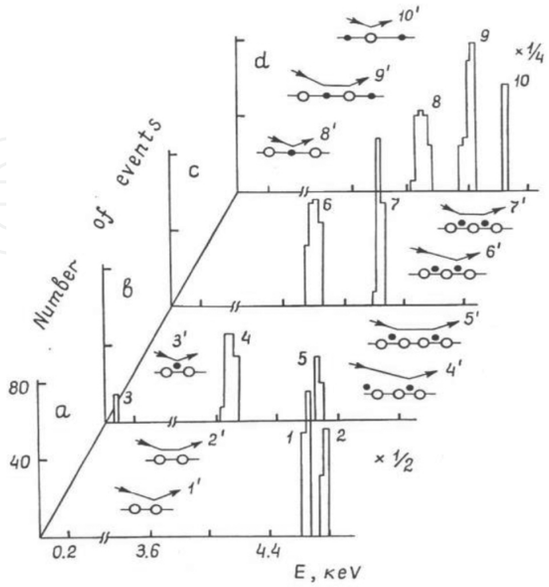

Figure 11. Histograms of energy distributions of 5 keV Ne^+ ions, undergoing specular scattering on a clean Ni(100) surface (a) and one covered by adsorption structures of oxygen p(2 × 2) (b) and c(2 × 2) (c), as well as on nickel oxide NiO (d). The sliding angle is ψ = 12.5°.Typical trajectories of scattered ions numbered 1'–10', contributing to corresponding peaks (1–10) are schematically presented.

Two peaks of the QS-scattering of ions on lighter adatoms were observed experimentally in ref. [46]. The third peak (5) is provided by QD-scattering on oxygen adatoms. In the energy spectrum for structure c(2 × 2)–O (Figure 12c), peaks of QS- and QD-scattering (6,7) on oxygen atoms with impact parameters p larger than $p_{\lim}$ are presented. The energy distribution of ions scattered on nickel oxide (Figure 2d) differs greatly from the distributions for chemisorption structures (Figure12b and c): peaks 8 and 10 correspond to QS0 scattering from oxygen and nickel atoms, and peak 9 between them correspond to QD-scattering from oxygen and nickel atoms. The analysis of the calculated spectra follows the fact that a number, intensity, and position of peaks on energy scale, corresponding to scattering on different adsorption structures, are different, which gives an opportunity to interpret them by means of comparison with experimental spectra. In **Figure 12**, calculated angular distributions of Ne^+ ions with E_0 = 5 keV and ψ = 12.5°, scattered from a clean Ni(100)<100> surface and one covered by different adsorption structures of oxygen are presented. In the case of a clean surface, the usual two-peak structure of angular distribution is observed [4, 5]. With the transition to the p(2 × 2)–O structure (**Figure 12b**), angular distribution of scattered ions changes considerably: it broadens to both sides, and in addition to the peaks observed from a clean surface, a peak appears at a limited angle of scattering from oxygen adatoms $\theta = \theta_{\lim}$ = 52.5° and a peak of oxygen recoil atoms at θ = 78° (hatched part). The peak at $\theta_{\lim}$ is provided by rainbow scattering, and its position on the angular scale gives an opportunity to identify the type of adatoms by the formula $m_2 = m_1 + \sin\theta_{\lim}$.

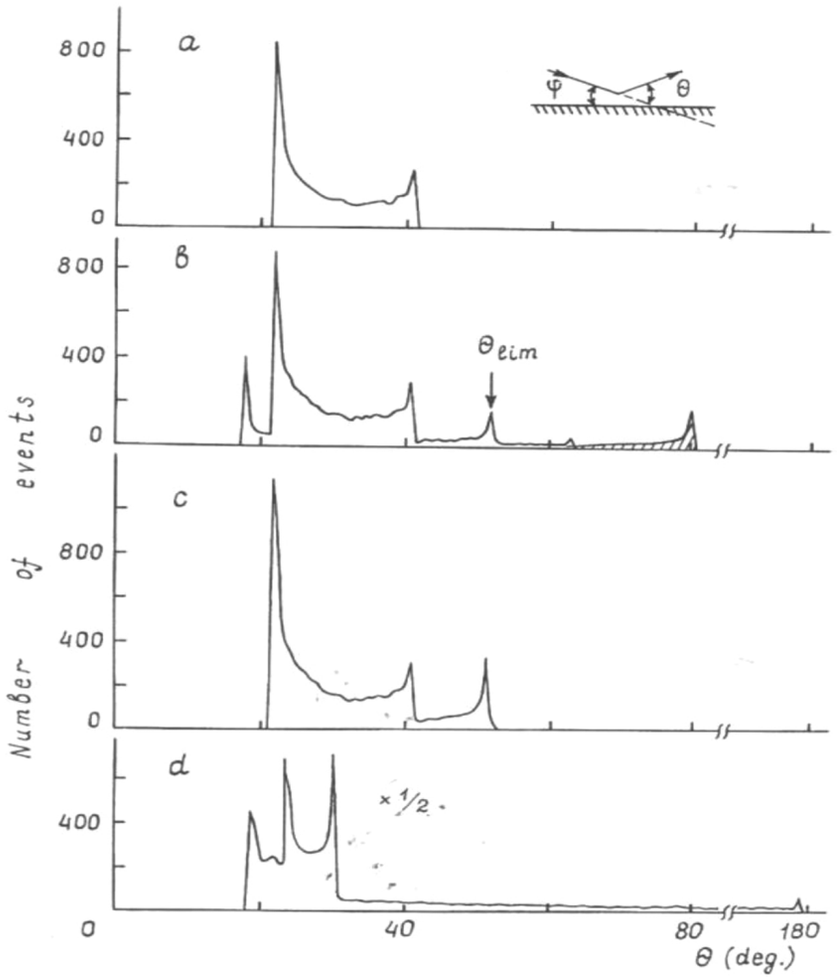

Figure 12. Angular distributions of 5 keV Ne^+ ions and ψ = 12.5°, scattered on a clean Ni(100)<100> surface (a) and covered by adsorption structures of oxygen p(2 × 2) (b) and c(2 × 2) (c), as well as nickel oxide NiO (d). The hatched field in the distribution for the structure p(2 × 2) is the contribution of primary knocked out oxygen adatoms.

Oxygen recoil adatoms are formed by the mechanism of direct knockout, and its detection allows the determination of the type of adsorbate and adsorption stage. At further exposure to oxygen and formation of c(2 × 2)–O chemisorption structure on the Ni(100) surface (**Figure 12c**), peaks at θ_{lim} and oxygen recoil atoms disappear. This is connected with the impossibility of QS-collisions of Ne^+ ions with oxygen adatoms with impact parameters $p < p_{lim}$ and releasing of recoil adatoms outside. The angular distribution as a whole narrows in comparison with the distribution for previous structures, testifying to the formation of a denser adsorption structure. On the formation on the surface of nickel oxide, the angular distribution of scattered ions (Figure 12d) also changes: the main structure of the distribution (three peaks) is located in a narrow field and has a background, spreading out to 180°. Such sharp broadening of the distribution is the characteristic feature for scattering on chains, consisting of different sort atoms. Thus, peculiarities of the chain effect at direct and inverse mass ratio of colliding particles and rainbow effect at QS- and QD-scattering of ions, heavier than adatoms lead to the appearance of characteristic peaks in the energy and angular distributions of ions, undergoing small-angle correlated scattering on chains of adatoms and target atoms. Analysis

http://dx.doi.org/10.5772/62731

of these peaks and comparison with experiment give an opportunity to control the initial stages of adsorption and identification of adsorption structures with the help of low-energy ion scattering.

4.5. Investigation of the dynamics of changes of the $Cu_3Au(100)$ surface in the course of ordering by low-energy ion scattering

$Cu_3Au(100)$ single crystal exhibits an order–disorder phase transition into the bulk at $T_c = 663$ K. This bulk transition is first-order. Theoretically it is predicted that the transition at the surface is of a different type than in the bulk [47, 48]. The transition at the surface has been intensively studied in recent years, including by time-of flight-ion scattering spectroscopy (TOF-ISS) method [49, 50]. In ref. [49] has been shown how the order–disorder transition modifies the atomic sequences in atomic rows, then changing the double-scattering conditions. The atomic row effect exhibits remarkable features in small-angle ion scattering from a single-crystal surface of complex composition when the rows in certain crystallographic directions consist of alternating atoms of different species. In this section $Cu_3Au(100)$ alloy surface has been investigated with low-energy ion scattering at temperatures below and above the bulk order–disorder transition temperature [51].

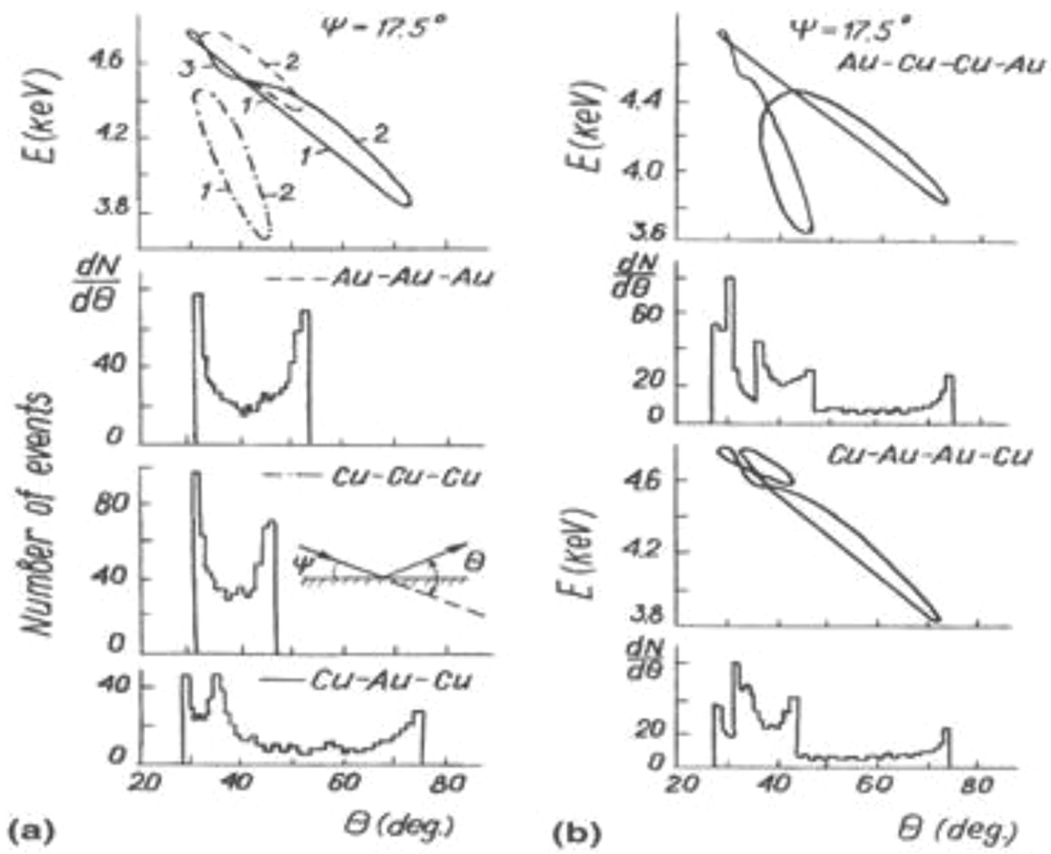

Figure 13. (a) Ovals of Ar^+ ion energy dependence on scattering angle θ and angular distributions at scattering from <110> atomic rows on Cu(100)-chain curve; Au(100)-broken curve, and $Cu_3Au(100)$-full curve; (b) Same dependencies for cases where one of the alloy atoms occurs twice in the row.

At temperatures $T > T_c$, all lattice sites are populated uniformly by atoms of both species, while at lower temperatures nonuniform occupation of sites by atoms of different species is typical. Note that <100> rows contain either only Cu or only Au atoms, whereas in the <110> rows the Cu and Au atoms alternate. **Figure 13a** presents ovals depicting the dependence of the energy of scattered Ar^+ ions with initial energy E_0 = 5 keV on the scattering angle θ, which consist of quasi-single (QS)—1 and quasi-double (QD)—2 scattering branches. Shown in the bottom panel are the corresponding angular distributions of ions scattered from <110> rows in the Au(100), Cu(100), and $Cu_3Au(100)$ planes. The dashed ovals correspond to the Au atoms, the chain one to the Cu atoms, and the solid oval with a characteristic break (3) to a row of alternating Cu and Au atoms. In the case of a mixed row, the oval has an unusual shape in that the QD branch is replaced by quasi-triple scattering (3) from a sequence of Au–Cu–Au atoms with the principal deflection from the Cu atom which results in considerable energy losses. The QS- and QD-scattering occur in this case primarily from Au atoms. The angular distribution contains in the region, corresponding to the break in the oval, an additional maximum and exhibits a dramatic broadening. The maximum appears as a shoulder at ψ = 15°, grows with increasing grazing angle, and exceeds in height at ψ = 19° the maxima at the limiting scattering angles. As follows from the calculation, the additional maximum comes from the rainbow effect associated with the enhanced scattering close to the shadow-cone boundary of the Au atom toward the nearest Cu atom in a narrow impact parameter region along the row.

Figure 13b shows also the scattering ion energy versus the scattering angle ovals and the corresponding angular distributions; however, in this case, in the alternating sequence of atoms, one of them, either Au or Cu occurs twice in succession. Both the energy ovals and the angular distributions are seen to vary dramatically. It is shown when two neighboring atoms belong to the same species, the characteristic break (3) transforms into an additional oval which lies lower than the principal one and corresponds to QS- and QD-scattering from a pair of Cu atoms. To this oval correspond two additional maxima in the angular distribution. A similar pattern is also observed in the case when two Au atoms adjoin one another in a mixed row. The relative height of the additional maxima was found to depend on the number of neighboring atoms of the same species in a row. Increasing the number of neighboring identical atoms up to three or more results in an increase of the corresponding additional maxima in the angular distribution. Note that the shape of the energy oval and the interval of possible scattering angles are retained, whereas relative height of the maxima at the limiting scattering angles decrease. The characteristic structure of the angular distribution with the number of maxima is also retained when thermal vibrations of atoms in the alloy are included. Thus, a comparison of the angular and energy distributions of ions scattered from the surface of an alloy in the process of ordering with similar distributions for pure targets made up of the alloy components permits a conclusion that two or more neighboring atoms in an alternating sequence are of the same species. The results obtained can be used to study a short-range order in alloys undergoing ordering.

4.6. Ion sputtering of single-crystal surfaces

In this section, the grazing ion sputtering processes of Si(001), SiC(001), and $Cu_3Au(001)$ surfaces at 0.5–5 keV Ne^+ bombardment have been studied by computer simulation [52, 53].

Sputtering has been simulated in the primary knock-on regime. Only the primary knock-on recoil (PKR) atoms ejected from first, second, and third layers have been considered. The presence of planar potential energy barrier on the surface was taken into account. The number of incident ions is 4×10^4. Each new particle is incident on a reset, pure surface. The incident ions and the recoil atoms were followed throughout their slowing-down process until their energy falls below a predetermined energy: 25 eV was used for the incident ions, and the surface-binding energy was used for the knock-on atoms. The calculations were performed on the crystals comprising up to 120 atomic layers. The initial energy of incident ions was varied from 0.5 to 5 keV, an angle of incidence ψ counted from target to the surface was 0–30°, and an azimuthal angle of incidence ξ realized by rotating the target around its normal and counted from the <100> direction was 0–180°.

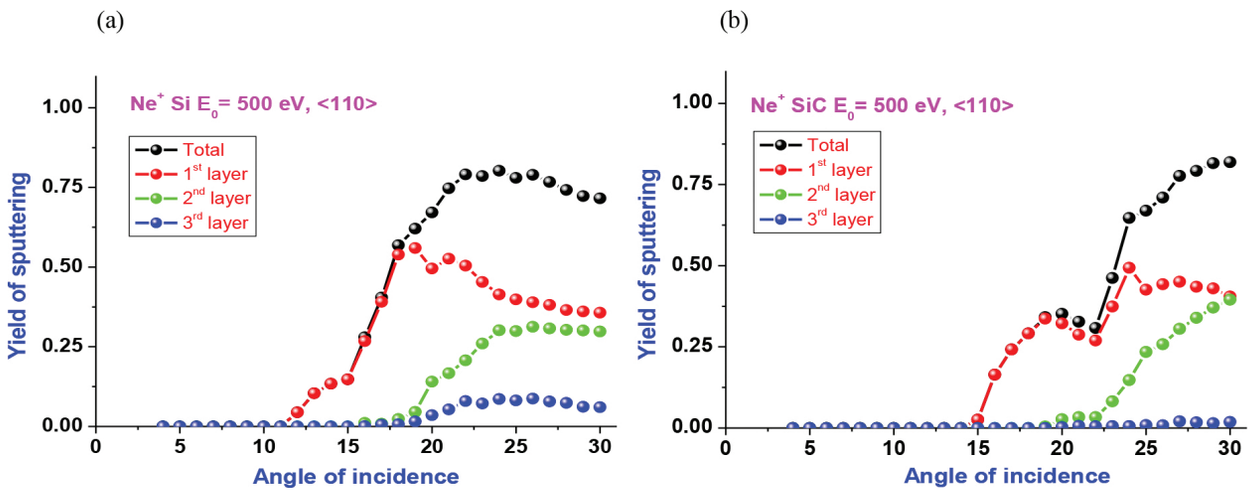

Figure 14. Sputtering yield of Si(001) (a) and SiC(001) (b) versus angle of incidence at Ne^+ ion bombardment.

In **Figure 14a,b** the angular dependences of the sputtering yield for Si(001) and SiC(001) surfaces subdivided into sputtering by the first three surface layers at 0.5 keV Ne^+ ion bombardment are compared. Note the angle of incidence ψ is counted from the surface. It is seen that there is a threshold angle of sputtering in all dependences. At angles of incidence less than the threshold angle, the incident ions cannot penetrate into the crystal and cannot eject target atoms. The threshold angle shifts to the lower values of angle of incidence with increasing the energy of incident ions. At ψ large than a threshold angle, with increasing ψ the number of PKR at first rises and achieves its maximum. There is a plateau (shorter for Si and wider for SiC) near the threshold angle because of insufficient ion energy for both long moving ions within surface semichannels and their penetration to deeper layers. With increasing the initial energy, this plateau disappears, and the sputtering yield decreases at large ψ. This decreasing of PKR yields is explained by partial penetration of ions into deeper layers and domination of the cascade sputtering mechanism. It is clear that the relative contributions of each layer to the total PKR yield strongly depend on the angle of incidence. In the angular range of ψ = 11–20° for Si and 15–23° for SiC, the sputtering occurs only from the first layer.

It is seen that the threshold angle is a bit smaller in the case of Si than for SiC. As results for high initial energy show, in general the sputtering yield is large in the case of SiC. These dependences allow choosing an angle of incidence for an effective sputtering at given initial energy. In **Figure 15a,b**, the sputtering yields of Si(001) and SiC(001) surfaces subdivided into sputtering by the first three surface layers versus the energy of incident Ne^+ ions are shown at ψ =10°. The threshold energy of sputtering is about 1 keV for these cases. There is more drastic increase of sputtering yield in the beginning of dependences for Si than for SiC. It is seen that the main contribution to the total sputtering comes from the sputtering of the first layer. Moreover, in the energy range of 0.5–1.5 keV for Si and 1–3 keV for SiC, the sputtering occurs only from the first layer. Further increasing of the ion energy results in increasing the contribution from second and third layers. The contribution to sputtering from the third layer is larger than the one from the second layer, as the atomic rows in the second layer lies directly under the one of the first layers in the <110> direction. Two local maxima at 2.5 and 4 keV are observed in the total sputtering yield dependence in the case of Si. Sputtering from the first layer gives a basic contribution to the first maximum, while the second maximum is formed by atoms ejected from the second and third layers. In the case of SiC the maximum of total dependence is formed by atoms ejected from the second layer. These results show that by choosing an angle and an energy of incidence, one can produce layer-by-layer sputtering of Si(001) and SiC(001) surfaces.

In **Figure 16**, the sputtering yield of $Cu_3Au(001)$ versus polar (ψ) and azimuth (ξ) angle of incidence at 5 keV Ne^+ ion bombardment is presented. Azimuthal angular dependence is shown only for the range of ξ = 0–90° due to its symmetricity. The main maxima at ξ = 0 and ξ = 90°, two local maxima at ξ = 35° and ξ = 55°, and deep minimum at ξ = 45° are observed in low crystallographic directions and near them. They are caused by the existence of original semichannels and channels in these directions. In these directions the incident ions either penetrate deeper into crystal or undergo the surface semichanneling. Due to ion channeling, the multiple collisions of projectile with target atoms are possible resulting in an intensive surface sputtering. Besides, the sputtering yield of $Cu_3Au(001)$ is two times less than one for SiC(001). These results show that influence of crystal orientation to sputtering yield depends on both crystal structure and its composition.

(a) (b)

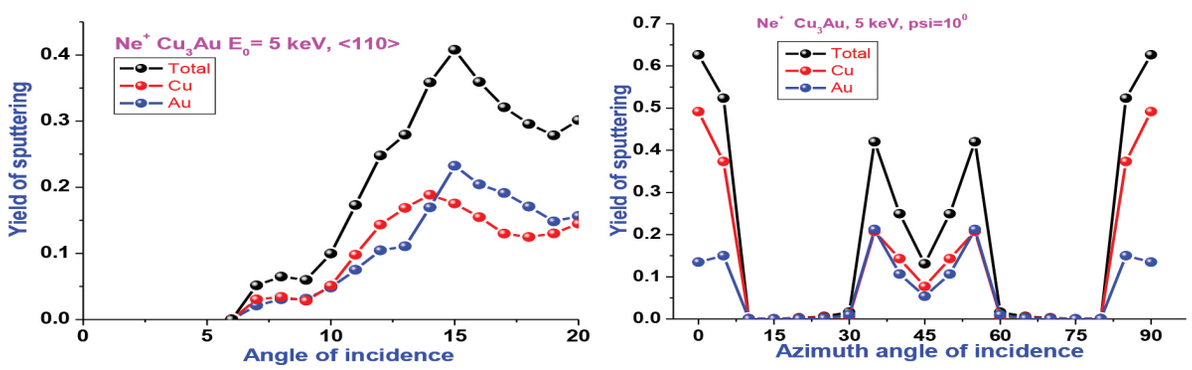

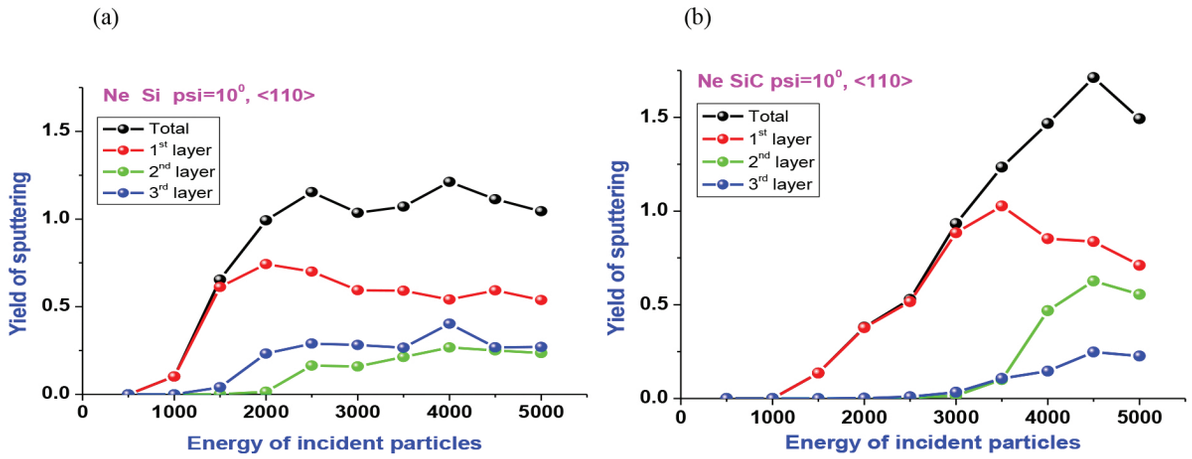

Figure 15. Sputtering yield of Si(001) (a) and SiC(001) (b) versus energy of incident Ne^+ ions at ψ =10°.

Figure 16. Sputtering yield of $Cu_3Au(001)$ versus polar (a) and azimuth (b) angle of incidence at E_0 = 5 keV.

Thus, the peculiarities of formation of PKR atoms at grazing ion incidence beam on an atomically smooth surface of a single crystal promotes its layer-by-layer sputtering. For the realization of the layer-by-layer sputtering mechanism, it is nessesary that a part of the ion energy, corresponding to the normal components of its velocity, will be lower than a threshold of sputtering of atoms of a layer, next to the surface one, that is, $E_i \sin^2 \psi_i < E_d$, where E_i is the ion energy before the *i*th collision, ψ_i is the angle between the ion movement direction and the semichannel axis before the *i*th collision, and E_d is the energy of displacement of atoms of a second layer (in the case considered, the bottom chain of semichannel). In these conditions it is possible to achieve successive removal of layers without disturbance of the next layer at removal of the previous one. Ion bombardment at grazing angles reduces considerably the influence of effect of crater walls and ion mixing on the results of layer-by-layer analysis, and increases its accuracy and sensitivity.

Parameters of single crystals (lattice parameter, binding energy, and mass of atoms) influence significantly the angular and energy dependences of sputtering yield. In general, the sputtering yield of the SiC(001) surface is larger than the one of the Si(001) surface. The proposed mechanism of layer-by-layer sputtering of a single-crystal surface at ion bombardment under grazing angles needs detailed checking and investigation by computer simulation as well as on experimental basis.

4.7. Determination of adatom sort and adsorption sites on single-crystal surfaces by ions channeling through thin films

Determination of the equilibrium adsorption sites of atoms adsorbed on crystalline surfaces and initial stages of adsorption is a fundamental problem in surface physics. Stensgaard [54] was the first to propose for the determination of the adsorbed site of D atoms adsorbed on the rear (100) surface of a thin Ni single crystal, 800 keV He^+ ions which channel through the sample. The adatoms were detected by monitoring the yield of the D(^{3}He,p) ^{4}He reaction. In the present section, we propose for the determination of the adsorption site and sort of light

adatoms on the rear surface of a thin crystal to use interaction with these adatoms of low energy ions of mass m_1 greater than the adatom mass m_2, channeling through the crystal. For $m_1 > m_2$, there exist a limiting angle $\theta_{\lim} = \arcsin(\mu)$, where $\mu = m_2/m_1$, which leads to the rainbow effect in scattering, that is, enhanced reflection that results in the appearance in the angular and energy distributions of transmitted ions of characteristic peaks useful for diagnostics purposes. In order to improve the usefulness of the angular and energy distributions of transmitted particles for diagnostic purposes, it can be recommended to also employ, besides the rainbow effect, the flux peaking phenomenon, that is, a spatial redistribution of the channeling particles in the transverse channel plane, which produces an increase of the flux in the central part of the channel and its sharp decrease on its periphery [56]. The sort and adsorption site of the adatoms are determined from the rainbow effect in the angular distributions of transmitted particles caused by their interaction with adatoms above the rear surface of the crystal [55, 56].

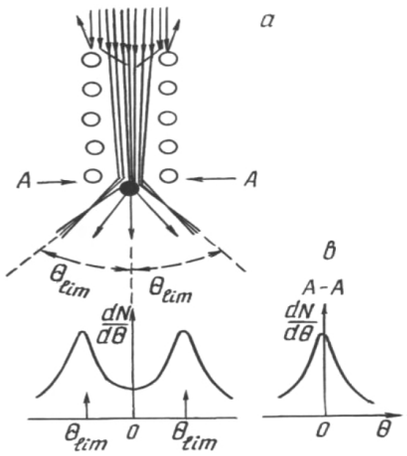

Figure 17. (a) The possibility of using the channeling effect to detect the adatom adsorption site above the rear crystal surface along the principal axes. (b) The changes in the angular distribution of the redistributed transmitted flux caused by the ion interaction with the adatom.

The trajectories of 1–5 keV He^+ and Ne^+ ions channeling in thin (Δz = 100–500 Å) Ni(100) films were computer-simulated in the binary collision approximation using the universal Biersack–Ziegler–Littmark potential and with the inclusion of elastic and inelastic energy losses. For ions emerging out of the rear side of the crystal, one calculates the coordinates of the emergence points projected on a plane perpendicular to the channel axis, the total scattering angle (the angle between the initial and final ion directions), and the final ion energy. Next, one calculates the interaction of the transmitted ions with the adsorbed atoms residing in various positions relative to the channel axis and at given heights h with respect to the rear surface of the crystal. The adatom sort and adsorption site are determined from a comparison of the angular distributions of the transmitted ions with or without adatoms present on the crystal surface (Figure 17a,b). **Figure 17a** illustrates the possibility of using the channeling effect to detect the adatom adsorption site above the rear crystal surface along the principal axes. **Figure 17b**

http://dx.doi.org/10.5772/62731

shows schematically the changes in the angular distribution of the redistributed transmitted flux caused by the ion interaction with the adatoms. We readily see that the presence of a peak in the angular distribution at the limiting scattering angle permits the identification of the adatom sort. Thus, the present method is efficient only when $m_2 < m_1$, that is, when the adatoms are lighter than the channeling ions. By choosing properly the ion energy and crystal thickness, one can obtain angular distributions with the main peak corresponding to the limiting scattering angle.

This is illustrated in **Figure 18**, showing angular distributions of 1 keV Ne^+ ions channeling through thin (Δz = 100 Å) Ni(100) films along <100> in the (a) absence and (b) presence of adatoms of carbon and (c) oxygen located at the channel center at a height h = 0.9 Å above the rear crystal surface, which were calculated for T = 0 K. The presence of adatoms affects noticeably the distributions in that they shift toward scattering angles $\theta \approx \theta_{lim}$, their main peaks corresponding to rainbow scattering (θ_{lim} = 35° for carbon and θ_{lim} = 50° for oxygen). The essential advantage of this method lies in its capability of detecting of very light adatoms, such as hydrogen and deuterium. Thickness of the film, channeling direction, and particle energy have influence only on the magnitude of these maxima, but not on their positions. Thus, this method allows discrimination between the isotopes of an adsorbed element. Similar arguments are valid also for close isotopes of carbon and oxygen. Thus, when $m_1 > m_2$, the angular distributions of transmitted ions allow a correct determination of the adatom sort. The film thickness is not a critical factor in this technique, and it can be taken thicker if one increases correspondingly the initial energy of ions.

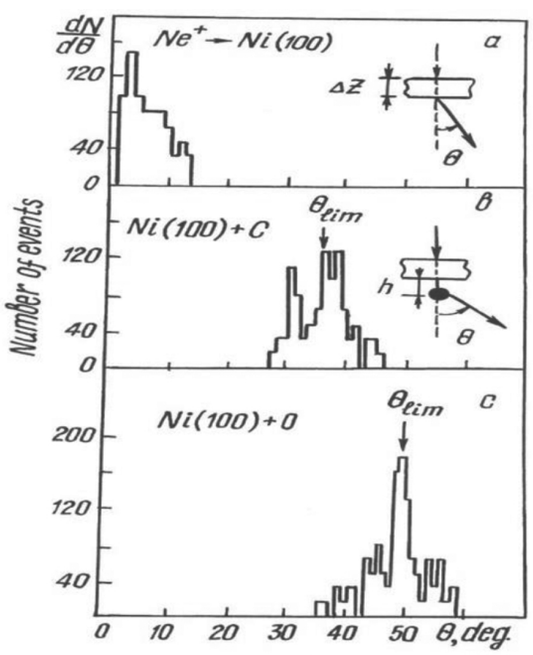

Figure 18. Angular distributions of 1 keV Ne^+ ions channeling through thin Ni(100) films in (a) absence and (b) presence of adatoms of carbon and (c) oxygen.

It is thought that rapid progress of the nanostructures physics and ultra-high vacuum technology allow to obtain in near future single-crystal films only a few hundred Angstroms thick with clean entrance and exit surfaces and well-ordered adsorbate structure on them. It was shown that the magnitude of main maximum at $\theta \approx \theta_{\lim}$ depends on the height h of the adatom above the crystal surface. For the case $Ne^+ \rightarrow Ni(100) + O$, where film thickness ($\Delta z$ = 100 Å) and E_0 = 1 keV, maximum occurs at h = 0.9 Å, which is in agreement with the experimental value [57]. The sensitivity of the angular distributions of transmitted ions to shadowed adatom positions which do not correspond to the channel center in the given direction can be revealed by varying the direction of particle channeling. The accuracy with which the adatom adsorption site with respect to the unit cell in the transverse plane of the channel can be determined is evaluated as ~0.1 Å. An experimental test of this technique would permit a realistic evaluation of its capabilities.

5. Conclusion

One can draw the following conclusions on the basis of the conducted researches:

- A considerable influence of the binding of surface atoms to each other on the process of ion scattering in the low-energy range by polycrystal targets is experimentally established.
- The elastic energy losses are considerably smaller than the inelastic ones in a region of glancing ion scattering. The predominance of the inelastic energy losses should reveal itself in the efficiency of the various inelastic processes accompanying the glancing ion scattering on a single-crystal surface.
- From the comparison of the results of computer simulation of the scattered particle trajectories with the experimental energy distributions, one can draw a conclusion that for bombardment of a Cu(100) surface with E_0 = 10 keV Ar^+ ions, isolated monoatomic steps consisting of several atoms (from one to four) are formed upon it. The distances between the steps vary from two lattice constants to ~45 Å.
- It was shown that the analysis of the characteristic peaks appearing in energy and angular distributions of ions undergoing small-angle correlated scattering on chains of adatoms and target atoms on the single-crystal surface and comparison with experiment gives an opportunity to control the initial stages of adsorption and identification of adsorption structures with the help of low-energy ion scattering.
- A comparison of the angular and energy distributions of ions scattered from the surface of an alloy in the process of ordering with similar distributions for pure targets made up of the alloy components permits a conclusion that two or more neighboring atoms in an alternating sequence are of the same species. The results obtained can be used to study a short-range order in alloys undergoing ordering.
- Sputtering yields of $Cu_3Au(001)$, Si(001), and SiC(001) surfaces versus the initial energy of incident ions (E_0 = 0.5–5 keV), angle of incidence (ψ = 0–30°), and azimuth angle of incidence

(ξ = 0–180°) have been calculated at Ne ion bombardment. It was shown that effective and layer-by-layer sputtering is possible near threshold angle and energy sputtering. The obtained results allow to select the optimum conditions for obtaining implanted depth distributions with demanded shape in narrow near-surface regions (5–10 atomic layers) of crystals.

- It was shown that the sort and adsorption site of the adatoms one can determined by the instrumentality of the rainbow effect in the angular distributions of transmitted channeled particles provided by their interaction with adatoms above the rear surface of the crystal. The accuracy with which the adatom adsorption site with respect to the unit cell in the transverse plane of the channel can be determined is evaluated as ~0.1 Å.

Author details

Farid F. Umarov[1*] and Abdiravuf A. Dzhurakhalov[2]

*Address all correspondence to: farid1945@yahoo.com

1 Kazakh- British Technical University, Almaty, Kazakhstan

2 University of Antwerp, Middelheimlaan 1, Antwerp, Belgium

References

[1] Van Hove MA *Surf. Sci*., 603, 1301–1305 (2009).

[2] Begemann, SHA, Boers, AL *Surf. Sci.*, 30, 134 (1972).

[3] Parilis, ES, Turaev, NYu, Umarov, FF *Radiat. Eff.*, 24, 207 (1975).

[4] Mashkova, ES, Molchanov, VA *Medium Energy Ion Reflection from Solids*. North-Holland Publ., Amsterdam (1985).

[5] Parilis, ES, Kishinevsky, LM, Turaev, NYu, Baklitzky, BE, Umarov, FF, Verleger, VKh, Niznaya, S., Bitensky, IS. *Atomic Collisions on Solid Surfaces*. Elsevier, North-Holland Publ., Amsterdam (1993).

[6] Smith, DP *Surf. Sci.*, 25, 171 (1971).

[7] Labanda JGC, Barnett SA, *J. Electron. Mater*., Sep (1997).

[8] Dzhurakhalov AA *Nucl. Instrum. Methods Phys. Res. B* . , 216, 202 (2004).

[9] Umarov FF, Dzhurakhalov AA, Teshabaeva NA *Appl. Surf. Sci.*, 125, 226 (1998).

[10] Roth J., Bohdansky J., Poschenrieder W., Sinha MK *J. Nucl. Mater.*, 63, 222–229 (1976).

[11] Bischoff L., Teichert J., Heera V. *Appl. Surf. Sci.*, 184, 372 (2001).

[12] Kim JC, Ji J-Y, Kline JS, Tucker JR, Shen T-C *Appl. Surf. Sci.*, 220, 293 (2003).

[13] Ecke G., Kosiba R., Kharlamov V., Trushin Yu., Pezoldt J. *Nucl. Instrum. Methods Phys. Res. B* 196, 39 (2002).

[14] Brown A., George H. B., Aziz M. J., Erlebacher J. *Mater. Res. Soc. Symp. Proc.*, 792, R7.8.1 (2004).

[15] Morgan DV. (Ed.). *Channeling Theory Observation and Applications*. Wiley, London (1973).

[16] Ziegler JF, Biersack JP, Littmark U. *Stopping and Ranges of Ions in Matters*. Pergamon, New York (1983).

[17] Kumakhov MA, Komarov FF *Energy Loss and Ion Ranges in Solids*. Gordon and Breach, New York (1981).

[18] Stepina NP, Kachurin GA *Sov. Phys. Semicond.*, 17, 449 (1983).

[19] Vavilov VS.. *Usp. Fiz. Nauk.*, 145, 9 (1985).

[20] Umarov FF, Rasulov AM, Khaidarov A. Kh. *Radiat. Eff. Defects Solids.*, 158, 481 (2003).

[21] Robinson MT, Oen OS *Phys. Rev.*, 132, 2385 (1963).

[22] Barret JH *Phys. Rev.*, 166, 219 (1968).

[23] Lindhard J. *Usp. Fiz. Nauk.*, 99, 240 (1969).

[24] Umarov FF, Bazarbaev NN, Kudryashova LB, Krylov NM *Nucl. Instrum. Methods Phys. Res. B.* , 196, 155 (2002).

[25] Umarov FF, Bazarbaev NN, Djyrabekova FG *Appl. Surf. Sci.*, 255, 6918 (2009).

[26] Algra AJ, Luitjens SB, Suurmeijer EPThM, Boers AL, *Appl. Surf. Sci.*, 10, 273 (1982).

[27] Robinson, MT, Torrens, IM *Phys. Rev.*, B9, 5008 (1974).

[28] O'Connor DJ, Biersack JP *Nucl. Instrum. Methods Phys. Res. B.,* 15, 14 (1986).

[29] Dzhurakhalov AA, Umarov, FF *Nucl. Instrum. Methods Phys. Res. B.*, 161–163, 377 (2000).

[30] Umarov FF, Bazarbaev NN, Kudryashova LB, Krylov NM *Nucl. Instrum. Methods Phys. Res. B.,* 196, 155 (2002).

[31] Umarov FF, Bazarbaev NN, Djyrabekova FG *Appl. Surf. Sci.*, 255, 6918 (2009).

[32] Landau LD, Lifshiz LM *Mechanica, Nauka* (1998) (in Russian).

[33] Pugacheva TS, Djurabekova FG, Miyagava Y., Valiev S. Kh. *Nucl. Instrum. Methods Phys. Res. B.,* 127–129, 260 (1997).

[34] Djurabekova FG, Umirzakov BE, Umarov FF, Miyagava Y. *Nucl. Instrum. Methods Phys. Res. B.*, 206, 194 (2003).

[35] Ziegler JF, Biersack JP, Littmark U. *The Stopping and Ranges of Ions in Solids*. Pergamon Press, New York (1985).

[36] Nizhnaya SL, Parilis ES, Verleger V.Kh *Radiat. Eff.*, 40, 23 (1979).

[37] Evdokimov IN, Webb RP, Armour DG, Karpuzov DS *Radiat. Eff.*, 42, 83 (1979).

[38] Dzhurakhalov AA, Umarov, FF *Nucl. Instrum. Methods Phys. Res. B.*, 136–138, 1092 (1998).

[39] Evdokimov IN, Mashkova ES, Molchanov VA *Dokl. Akad. Nauk SSSR.*, 186, 549 (1969).

[40] Luitjens, SB, Algra, AJ, Suurmeijer, EPThM, Boers, AL *Surf. Sci*. 100, 315 (1980).

[41] Umarov, FF, Parilis ES, Dzhurakhalov AA *Vacuum*, 44(9), 889–891 (1993).

[42] Dzhurakhalov AA, Kutliev UO, Umarov FF *Radiat. Eff. Defects Solids.*, 159, 293–299 (2004).

[43] Shulga VI *Radiat. Eff.*, 51, 1 (1980).

[44] Woodruff DP, Delchar TA *Modern Techniques of Surface Science*. Cambridge University Press, Cambridge (1986).

[45] Dzhurakhalov AA, Umarov, FF *Surf. Coat. Technol.*, 103, 16–19 (1998).

[46] Bastasz R., Felter TE, Ellis WP *Phys. Rev. Lett*., 63, 558(1989).

[47] Sanchez JM, Moran-Lopez JL *Surf. Sci. Lett*. 157, 297 (1985).

[48] Lipovsky R. *Phys. Rev. Lett*. 49, 1575 (1982).

[49] Houssian L., Bertrand P. *Nucl. Instrum. Methods Phys. Res. B.*, 118, 467 (1996).

[50] Houssian L., Bertrand P. *Nucl. Instrum. Methods Phys. Res. B.*, 115, 161 (1996).

[51] Dzhurakhalov AA, Umarov, FF *Nucl. Instrum. Methods Phys. Res. B.*, 161–163, 377 (2000).

[52] Umarov FF, Dzhurakhalov AA, Teshabaeva NA *Appl. Surf. Sci.*, 125, 226 (1998).

[53] Umarov FF, Dzhurakhalov AA *Surf. Interf. Anal*., 45(1), 83 (2013).

[54] Stensgaard I. *Nucl. Instrum. Methods Phys. Res. B.*, 15, 300 (1986).

[55] Dzhurakhalov AA, Parilis ES, Rasulov AM, Umarov FF *Poverkhnost*,6, 148 (1990)(in Russian).

[56] Umarov FF, Rasulov AM *Appl. Surf. Sci*., 135, 269 (1998).

[57] Demuth JE, Jepsen DW, Marcus PM *Phys. Rev. Lett*., 31, 540 (1973).

IntechOpen